

THE MOUSE PULSAR WIND NEBULA

NOEL KLINGLER¹, OLEG KARGALTSEV¹, GEORGE G. PAVLOV², C.-Y. NG³, PAZ BENIAMINI¹, IGOR VOLKOV⁴

¹The George Washington University, Department of Physics, 725 21st St NW, Washington, DC 20052

²Pennsylvania State University, Department of Astronomy & Astrophysics, 525 Davey Laboratory, University Park, PA 16802

³Department of Physics, the University of Hong Kong, Pokfulam, Hong Kong

⁴University of Maryland, College of Computer, Mathematical, and Natural Sciences, College Park, MD 20742

Draft version November 29, 2017

ABSTRACT

PSR J1747–2958 is a young ($\tau = 26$ kyr), energetic ($\dot{E} = 2.5 \times 10^{36}$ erg s $^{-1}$) supersonic pulsar at an estimated distance $d = 5$ kpc. It powers the Mouse pulsar wind nebula (PWN; G359.23–0.82), which consists of a pulsar tail spanning 12' in radio and 45'' in X-rays. We present the results of our analysis of *Chandra X-ray Observatory* ACIS and HRC observations of the pulsar and its X-ray nebula, as well as an analysis of archival lower-frequency data. The HRC image reveals a point-like source at the pulsar position at $\approx 1''$ from the bow shock apex of the PWN. The deep ACIS image and radio/ γ -ray pulse profiles indicate that the compact nebula is composed of a flattened equatorial outflow deformed by the ram pressure, and that the angle between the pulsar's spin axis and the line of sight is about 70°, while the magnetic dipole axis is inclined to the spin axis by about the same angle. The spatially-resolved spectral map of the X-ray tail shows that the photon index of the power-law (PL) spectrum increases from $\Gamma = 1.65 \pm 0.02$ to 3.0 ± 0.1 over the 45'' extent, while the spatially-averaged spectrum of the X-ray tail fits a single absorbed PL with $\Gamma = 2.09 \pm 0.03$. We detected the Mouse PWN in 150 MHz GMRT data and found evidence of its detection in 24 μ m *Spitzer* data. The radio and infrared data suggest that at low frequencies the spectrum of the X-ray-emitting region of the tail can be described by a broken PL with at least one spectral turnover between radio and X-ray frequencies. Using the multiwavelength data, we estimated a magnetic field $B \sim 100 - 200 \mu$ G in the tail, which is consistent with the rapid synchrotron cooling observed.

Keywords: pulsars: individual (PSR J1747–2958) — stars: neutron — X-rays: general

1. INTRODUCTION

Pulsars are among nature's most powerful particle accelerators, producing particles with energies up to a few PeV. As a neutron star rotates, it imparts its rotational energy into a magnetized ultrarelativistic particle wind, which encounters a termination shock (TS) downstream due to interactions with the ambient medium. Synchrotron emission can be seen downstream of the TS from radio to γ -rays as a pulsar wind nebula (PWN). The properties of PWNe, such as their appearance, spectrum, and radiative efficiency, depend on the pulsars' parameters (e.g., the spin-down power \dot{E} and the angle α between the magnetic and spin axes), as well as the pulsars' velocity and the properties of their environment (Kargaltsev & Pavlov 2008). If a pulsar moves through the interstellar medium (ISM) at a supersonic speed, the ram pressure exerted by the ISM balances that of the pulsar wind and forms a bow shock, which redirects and channels the wind in the direction opposite to that of the pulsar's motion, forming a pulsar tail (see Bucciantini et al. 2005, Gaensler & Slane 2006). Observations of fast-moving energetic pulsars in radio and X-rays have revealed such tails extending for parsecs behind the pulsars. In several cases, bright compact nebulae (CNe) with complex structures on small scales can be seen in the vicinity of the fast-moving pulsar. Studying the wind nebulae of supersonic pulsars provides information about the properties of pulsar wind (e.g., flow speeds and magnetization), particle acceleration regions, properties of the ISM and its interaction with pulsar wind, the pulsar magnetosphere geometry, and the distribution of veloc-

ities that neutron stars acquire during their progenitor supernovae.

G359.23–0.82 (“the Mouse” PWN) is a 12' long axisymmetric non-thermal nebula originally discovered in a Very Large Array (VLA) survey of the Galactic center (Yusef-Zadeh & Bally 1987). Subsequent observations have revealed a bow shock structure at the head of the nebula and its synchrotron nature (Yusef-Zadeh & Bally 1989). *ROSAT* observations later revealed X-ray emission at the head of the Mouse (Predehl & Kulkarni 1995). Follow-up observations with the Parkes radio telescope later identified the X-ray source as PSR J1747–2958: a relatively young (spin-down age $\tau_{\text{sd}} = 26$ kyr) and energetic ($\dot{E} = 2.5 \times 10^{36}$ erg s $^{-1}$) pulsar powering the nebula (Camilo et al. 2002). In radio, the bulbous CN and long narrow tail morphologically resemble the body and tail of a mouse, which gave rise to the PWN's nickname. Radio polarimetry of the CN has revealed a magnetic field perpendicular to the pulsar's motion direction ahead of the pulsar, and parallel to the velocity direction in the extended tail (Yusef-Zadeh & Gaensler 2005). A 36 ks *Chandra* ACIS-S observation of the Mouse PWN has revealed a 45'' long X-ray nebula and showed that its spectrum can be described by a power-law (PL) with a photon index that increases with distance from the pulsar (Gaensler et al. 2004; hereafter G+04), and the 53 ks *XMM-Newton* observation has shown the nebula has a spatially-averaged photon index $\Gamma \simeq 1.9$ (Mori et al. 2005). Pulsed γ -ray emission from PSR J1747–2958 has also been detected with the *Fermi* LAT (Abdo et al. 2013).

The distance to the Mouse is uncertain, with somewhat different values used by different authors. Observations of HI absorption showed that maximum distance of G359.23–0.82 is \sim 5.5 kpc (Uchida et al. 1992). The Galactic electron density model of Cordes & Lazio (2002) yields a distance of 2 kpc for the dispersion measure of the pulsar, $DM = 101.5 \text{ pc cm}^{-3}$ (Camilo et al. 2002), while the models of both Taylor & Cordes (1993) and Yao, Manchester, & Wang (2017) both suggest a distance of 2.5 kpc. G+04 noted that the hydrogen column density obtained from fits to the X-ray spectra, $N_H \approx 2.7 \times 10^{22} \text{ cm}^{-2}$, is much larger than the hydrogen column density implied by the the pulsar’s 2 kpc DM distance, $N_H \approx 4 \times 10^{21} \text{ cm}^{-2}$. Considering that the Galactic electron densities have large uncertainties in directions close to the Galactic center (since there are few pulsars in this direction to calibrate the electron distributions), G+04 suggest that the DM distance is unreliable. Using the radial profile of Galactic molecular surface density from Dame (1993), G+04 found that the observed N_H suggests the pulsar lies at a distance ~ 5 kpc. Therefore, here we also adopt the distance of 5 kpc as a reasonable estimate and will scale all distance-dependent quantities to this value. At this distance, the proper motion of the radio CN tip measured by Hales et al. (2009) implies a projected transverse space velocity of $306 \pm 43 \text{ km s}^{-1}$ eastward. In Table 1 we the list relevant pulsar parameters.

In this paper we present the study of a series of deeper X-ray observations of the Mouse PWN taken with the *Chandra X-ray Observatory* (CXO). In Section 2 we describe the observations and data reduction techniques used. In Section 3 we present X-ray and radio images of the PWN, spectral maps, and in-depth spectral fit results. In Section 4 we discuss the implications of our findings and examine the multiwavelength properties of the Mouse, and finally, in Section 5 we present our conclusions.

2. OBSERVATIONS, DATA REDUCTION, AND DATA ANALYSIS

Four \approx 30 ks observations of the Mouse PWN were carried out over the course of 16 months, from March 2013 to July 2014. The data were taken with the CXO’s ACIS-I instrument operating in Very Faint timed exposure mode (3.2 s time resolution). In our analysis we also used the archival 36 ks ACIS-S observation (ObsID: 2834; PI: Gaensler), which was taken in Faint timed exposure mode, and the archival 58 ks HRC-I observation (ObsID: 9106; PI: Ng). The details of these observations are summarized in Table 2. Only the ACIS observations are used for spectral analysis, as the HRC observation has (almost) no spectral information. It is worth noting that there is one additional archival *Chandra* observation which contains the Mouse within its field of view: ObsID 14596 (ACIS-S); however this observation is not used in our analysis as the Mouse was too far from the optical axis ($\sim 9'$) to allow any meaningful spectral or morphological analysis of the PWN (due to blurring caused by the much broader off-axis PSF, which would still preclude spatially-averaged spectroscopy of the PWN as it would be contaminated from the pulsar emission).

We used the *Chandra* Interactive Analysis of Observations (CIAO) software version 4.8 and CXO Calibration

Database (CALDB) version 4.7.0 for all data processing. All observations were reprocessed using `chandra_repro` to ensure that the latest calibrations are applied. For the ACIS observations, we applied boresight corrections to account for small systematic offsets between the observations. The corrections were determined by binning the ACIS images by a factor of 0.25 (of the native ACIS pixels of size $0''.492$), aligning the pulsar position¹ to that in the longest ACIS observation (ObsID 2834), and applying CIAO’s `wcs_update` to modify the WCS information in the file headers. To improve the absolute *Chandra* astrometry, we used `wcs_match` to minimize the positional offsets between the X-ray centroid positions of nearby field point sources (obtained by running `wavdetect` on the longest observation, ObsID 2834) and the positions of their 2MASS counterparts (within $1''$ of the X-ray sources). The resulting aligned astrometry-corrected images were used to produce the merged ACIS image shown in Figure 1 together with the HRC-I image. We created exposure maps for each observation and produced a merged exposure-map-corrected image with the `merge_obs` routine using the default effective energy of 2.3 keV. Spectra were extracted using the CIAO `specextract` tool and were fitted with absorbed power-law (PL) models in XSPEC with solar abundances assumed (we used the `tbabs` model, which uses the absorption cross sections from Wilms et al. 2000). For the ACIS observations, photon energies were restricted to the 0.5–8 keV range for all images and spectral analyses. All uncertainties listed below are at the 1σ confidence level unless specified otherwise.

To create the adaptively-binned spectral map, we use the weighted Voronoi tessellation (WVT) algorithm of Diehl & Statler (2006), which is a generalization of the Voronoi binning algorithm by Cappellari & Copin (2003). WVT is a method of adaptively binning two-dimensional data so that each bin (spatial region) meets a specified signal-to-noise ratio (S/N) requirement (i.e., the spatial resolution is maximized while a constant S/N is maintained across the spatial bins). Diehl & Statler (2006) developed a method to create adaptively-binned temperature maps of supernova remnants and galaxy clusters². We adapted their code for the creation of spectral maps of PWNe from non-adjacent (in time) ACIS observations. We applied all required observation-specific calibration corrections (as mentioned above) and performed simultaneous spectral fits for the same spatial region from different observations; this allowed us to use individual, observation-specific responses for each region. To create the WVT bins for the spectral map, we use the merged ACIS image binned by a factor of 0.5, and require a S/N of 30 for each WVT bin (spatial region).

Radio images were obtained from the NRAO VLA Archive Survey (NVAS; Crossley et al. 2007)³. The 150 MHz flux density was measured from the pipeline-processed image from the TIFR (Tata Institute of Fundamental Research) GMRT (Giant Metrewave Radio Tele-

¹ The centroid position was calculated using counts within an $r = 0''.55$ circle centered on the brightest pixel.

² The source code can be found at <http://www.phy.ohio.edu/diehl/WVT/>

³ <http://archive.nrao.edu/nvas/>

Table 1
Observed and Derived Pulsar Parameters

Parameter	Value
R.A. (J2000.0; radio position), α	17 47 15.882 (8)
Decl. (J2000.0; radio position), δ	-29 58 01.0 (7)
Epoch of position (MJD)	52613
Galactic longitude, l (deg)	359.31
Galactic latitude, b (deg)	-0.84
Spin period, P (ms)	98.8
Spin period derivative, \dot{P} (10^{-14} s s $^{-1}$)	6.132
Dispersion measure, DM (pc cm $^{-3}$)	101.5
Adopted distance, d (kpc)	5
Velocity, v_{\perp} (km s $^{-1}$)	306 ± 43
Spin-down power, \dot{E} (erg s $^{-1}$)	2.5×10^{36}
Spin-down age, $\tau_{\text{sd}} = P/(2\dot{P})$ (kyr)	25.5
Surface magnetic field, B_{surf} (G)	2.5×10^{12}

Parameters are from the ATNF catalog (Manchester et al. 2005, Camilo et al. 2002, G+04, and Hales et al. 2009). The values in parentheses are the last digit errors for the pulsar position.

Table 2
Chandra observations used in our analysis

ObsId	Instrument	Exposure (ks)	Date	θ (arcmin)
2834	ACIS-S	36.3	2002 Nov 19	1.23
9106	HRC-I	57.8	2008 Feb 07	0.26
14519	ACIS-I	29.7	2013 Mar 28	0.56
14520	ACIS-I	30.6	2013 Jul 25	0.58
14521	ACIS-I	27.8	2014 Mar 16	0.66
14522	ACIS-I	29.7	2014 Jul 25	0.68

θ is the angular distance between the pulsar and the optical axis of the telescope.

scope) Sky Survey (TGSS; Intema et al. 2017)⁴, and the infrared (IR) flux was measured from a pipeline-processed image from the *Spitzer* MIPSGAL 24 μ m Galactic Plane Survey (Gutermuth & Heyer 2015). We used the Python package *naima* (Zabalza 2015) to plot the multiwavelength spectra.

3. RESULTS

3.1. Spatial Morphology

The 118 ks *Chandra* data from the new observations offer a much deeper view of the Mouse PWN compared to the 36 ks observation described by G+04. The HRC and ACIS images, at their highest resolution, both reveal an interesting morphology within a few arcseconds of the pulsar. The head of the CN (i.e., the brighter area upstream (east) of the dashed line in Figure 1) displays a cometary shape with a “filled” morphology, but the front edge of the bright CN does not follow a simple parabolic shape (see the green-colored areas in Figure 1). The HRC-I image best shows the excess emission ahead of the pulsar (the emission east of the white-colored area coincident with the pulsar) accompanied by the rapid widening of the CN that is particularly pronounced north of the pulsar and seen up to about 4'' from it. The CN continues to widen up to about 10'' from the pulsar (in the direction opposite to that of the pulsar motion). This behavior abruptly changes beyond this distance, where

the nebula becomes fainter and narrower. The transition between the two regimes happens along the boundary which is shown by the inclined dashed line in Figure 1 (left panel) which has a position angle of 37° degrees East of North.

In Figure 2 we present the brightness profile of the PWN, obtained from the exposure-corrected merged ACIS image (using a 12'' × 100'' region with the longer dimension oriented along the east-west direction and centered on the pulsar in the transverse direction). Three distinct regimes can be identified in the brightness profile based on the change of the profile slope (shown by the straight orange lines in Figure 2). Note that the vertical scale is logarithmic and, therefore, a linear trend in the plot corresponds to an exponential (or nearly exponential) decay. The X-ray tail brightness fades to background levels approximately 50'' from the pulsar.

3.2. Spatially-Resolved Spectra

The sub-arcsecond resolution of *Chandra* allows us to perform spatially-resolved spectroscopy despite the small angular size of the PWN. We first explored the pulsar vicinity to see if there is any spectral evidence of the pulsar being detected and then characterized the spectral changes in the extended PWN. In all cases we simultaneously fit the spectra (0.5–8 keV) from all 5 ACIS observations of the Mouse PWN (since no significant spectral nor morphological changes are seen in the PWN between the observations). We obtained the background spectrum using a rectangular 138'' × 39'' region placed well outside the boundaries of both the X-ray and radio tails (centered at R.A.=17^h47'07".5, Decl.=−29°56'43".2, and excluding two faint field point sources), and subtracted it from the source spectra in all spectral fits.

3.2.1. Spectrum in the Pulsar’s Vicinity

To probe the pulsar’s spectrum, we used a small extraction region of radius $r = 0''.74$ (1.5 native ACIS pixels, corresponding to approximately a 90% encircled counts fraction⁵), centered at the brightest pixel when the merged image is binned by a factor of 0.5. The small aperture is intended to minimize the contamination from the nebula. The extracted pulsar spectrum was then fitted with an absorbed PL model which produced a good fit: $\chi^2_{\nu} = 1.09$ for $\nu = 99$ degrees of freedom (dof). The best-fit $N_{\text{H}} = (2.61 \pm 0.18) \times 10^{22}$ cm $^{-2}$ is consistent with the value previously reported by G+04 ($N_{\text{H},22} = 2.7 \pm 0.1$ cm $^{-2}$), and with the value found from fitting the entire X-ray tail ($N_{\text{H},22} = 2.8 \pm 0.07$ cm $^{-2}$, see Section 3.2.2), so we fixed $N_{\text{H},22} = 2.7$ for all subsequent fits. The fit of the pulsar’s spectrum yields photon index $\Gamma = 1.55 \pm 0.04$ and an absorbed X-ray flux of $(1.04 \pm 0.01) \times 10^{-12}$ erg s $^{-1}$ cm $^{-2}$. Attempts to fit the pulsar spectrum with a PL+blackbody (PL+BB) model with Γ frozen at 1.55 and a BB normalization corresponding to an $R = 10$ km NS at 5 kpc yields $kT = 131 \pm 27$ eV, but the fit quality is virtually the same as for the PL-only fit ($\chi^2_{\nu} = 1.10$ for $\nu = 98$), and the thermal component is therefore not statistically required by the data. We found an upper limit on the neutron star surface temperature by gradually increasing the temperature of the BB component

⁴ <http://tgssadr.strw.leidenuniv.nl/doku.php>

⁵ see http://cxc.harvard.edu/ciao/PSFs/psf_central.html

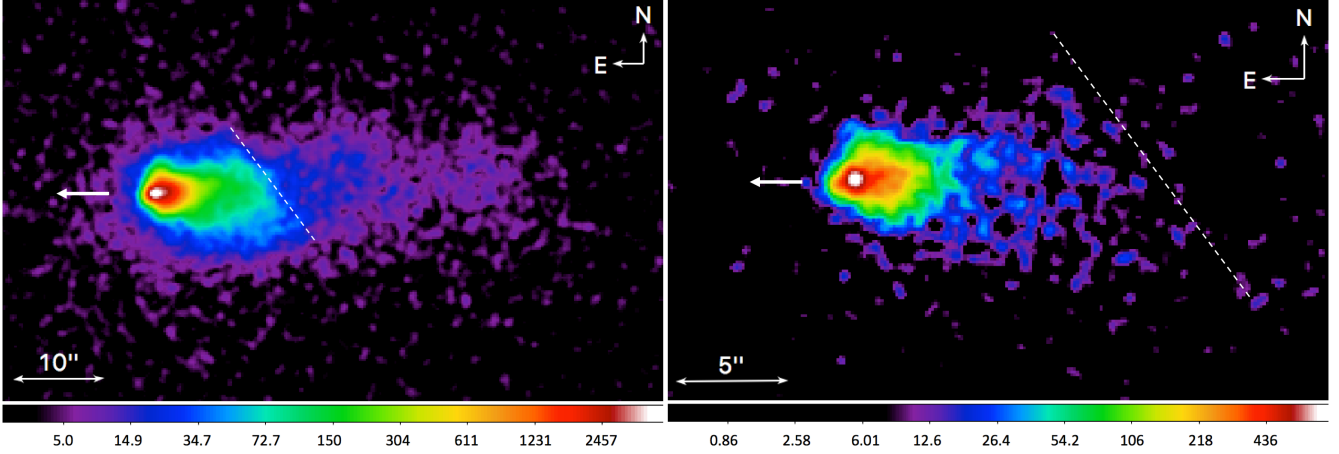


Figure 1. Left: Merged image from five ACIS observations (0.5–8 keV; the total exposure is 154 ks) with a pixel size of 0''.25 (a binning factor of 0.5 applied to the native 0''.492 pixels) and smoothed with an $r = 0''.75$ (3 pixel) Gaussian kernel. Right: Zoomed-in HRC-I image (58 ks; pixel size 0''.123) smoothed with an $r = 0''.37$ (3 pixel) Gaussian kernel. The white arrows show the direction of the pulsar’s proper motion (eastward) measured by Hales et al. (2009). The dashed white line (shown in both images) marks the sharp drop in surface brightness seen in the ACIS image.

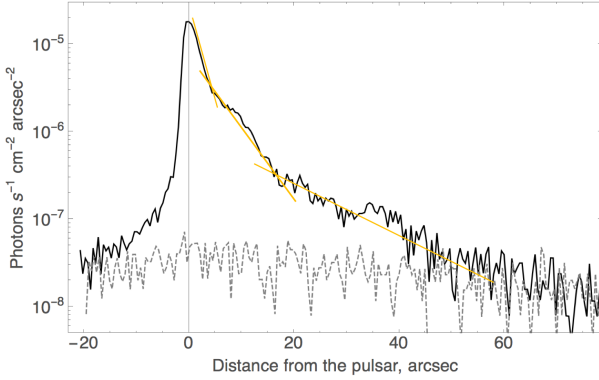


Figure 2. Linear brightness profile of the Mouse PWN obtained from the exposure-corrected image (in 0.5–8 keV), using a rectangular extraction region with a height of 12'' in the North-South direction (vertically centered on the pulsar) and a length of 80'' in the East-West direction (West being represented by positive distance values, and zero corresponding to the pulsar position). The dashed gray curve shows the background surface brightness, obtained using the same extraction region placed outside the PWN (20'' to the North). The orange lines are plotted over the brightness profile to highlight the three segments with different dependences of brightness on distance from the pulsar.

(and re-fitting the PL component at each new temperature) until the model became inconsistent with the data at the 3σ confidence level. This yields an upper limit $kT = 166$ eV ($T = 1.93$ MK).

3.2.2. PWN

We performed spatially-resolved spectroscopy for the rest of the PWN in several ways. We first followed the approach of G+04 and extracted spectra from regions enclosed within the brightness contours (we will call them “contour regions” below; see Figure 4). The spectra fitted with an absorbed PL model (see Table 3) exhibit substantial changes in the photon index, $\Delta\Gamma \approx 1$, between the inner and the outer contour regions (regions 2 and 6 in Figure 4). The two outermost contour regions (7 and 8 in Figure 4) were divided into two parts along the North-South line placed just ahead of the pulsar to determine if the spectrum changes ahead of the pulsar.

The inner head (within region 7) exhibits a significantly harder spectrum, $\Gamma = 1.54 \pm 0.16$, than that of the outer head (within region 8), which has $\Gamma = 2.61 \pm 0.15$.

To further investigate spectral softening with distance from the pulsar along the X-ray tail, we extracted spectra from 15 rectangular regions shown in Figure 4. Since the tail’s brightness decreases with distance, we used larger regions at the end of the tail to collect enough counts. We found that Γ increases nearly monotonically with distance, as seen in Figure 5. The photon index Γ in the outermost rectangular region is larger than that of the innermost one by $\Delta\Gamma \approx 1.4$. This variation is noticeably larger than that found for the contour regions (see Table 3), perhaps because the outermost regions include areas of harder spectra closer to the pulsar.

Fitting the spectrum of the entire X-ray tail (the dashed contour in Figure 3) produces a statistically acceptable fit with $\Gamma = 2.09 \pm 0.02$ and $\chi^2_\nu = 0.98$ for $\nu = 242$. This underscores the danger of inferring the slope p of the spectral energy distribution (SED) of the particles injected at the termination shock from the photon index $\Gamma = (p + 1)/2$ (for synchrotron radiation) obtained from a fit to the spectrum extracted from a large region of a PWN (a common choice for fainter PWNe necessitated by low count statistics; $p = 2\Gamma - 1$). Leaving N_H as a free parameter in the above fit yields $N_H = (2.80 \pm 0.07) \times 10^{22} \text{ cm}^{-2}$ (consistent with the value obtained above from fitting the spectrum from the pulsar vicinity), and $\Gamma = 2.14 \pm 0.04$ with $\chi^2_\nu = 0.97$ for $\nu = 241$ d.o.f.

Finally, in order to investigate the spectral variations within the Mouse PWN on even smaller spatial scales, we produced adaptively-binned spectral maps. The weighted Voronoi tessellation (WVT) approach varies the bin sizes which allows us to achieve the maximum spatial resolution for the specified S/N=30. We first binned the merged ACIS image into regions such that they have a minimum S/N of 30 (Figure 6, top panel)⁶ and then fit the spectra (from the five individual observations)

⁶ Some regions will have S/N > 30 since the addition of bright pixels to a region can place the S/N above the minimum

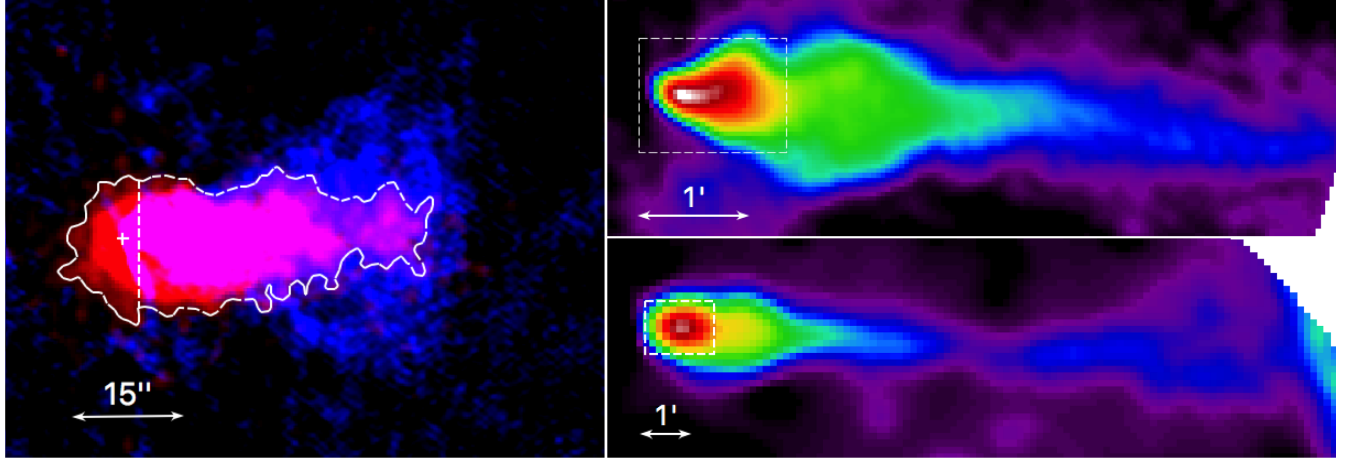


Figure 3. Left: Composite X-ray (red; binned by a factor of 0.5, and smoothed with an $r = 0''.74$ (3-pixel) Gaussian kernel) and radio (blue; VLA, 4.77 GHz, $1''.17 \times 1''.00$ beam) image of the Mouse PWN. The radio pulsar position is marked by the cross. The white contour encloses the X-ray nebula with the western (dashed) segment used to extract the entire tail spectrum (Section 3.3) and multiwavelength spectrum (Section 4). Right: VLA radio images (top: 4.89 GHz, $12''.4 \times 9''.8$ beam; bottom: 1.49 GHz, $34''.6 \times 30''.5$ beam) showing the extended tail of the Mouse. The field of view of the image on the left is shown by the dotted white box in the right panels. The radio images were obtained from the NRAO VLA Archive Survey (Crossley et al. 2007).

Table 3
Spectral Fits for Different Regions

Contour Region	Area (arcsec 2)	Net Counts, 0.5–8 keV	Counts per bin	Γ	\mathcal{N}_{-4}	$\chi_{\nu}^2 (\nu)$	$F_{X,-12}$	$L_{X,33}$
Pulsar	1.7	3785 ± 62	60	1.55 ± 0.04	3.01 ± 0.14	1.09 (99)	1.95 ± 0.03	5.83 ± 0.09
2	12.4	16803 ± 130	120	1.65 ± 0.02	8.10 ± 0.23	1.12 (120)	4.77 ± 0.05	14.3 ± 0.3
3	17.4	5223 ± 73	60	1.86 ± 0.04	3.05 ± 0.17	1.75 (68)	1.50 ± 0.04	4.48 ± 0.12
4	52.5	5390 ± 74	60	2.19 ± 0.04	4.78 ± 0.23	1.14 (74)	1.88 ± 0.04	5.62 ± 0.12
5	100.5	3380 ± 59	50	2.25 ± 0.05	3.10 ± 0.20	1.11 (52)	1.18 ± 0.05	3.53 ± 0.15
6	159.1	3145 ± 57	30	2.69 ± 0.05	4.44 ± 0.25	1.10 (91)	1.42 ± 0.06	4.25 ± 0.18
7 (inner head)	6.7	582 ± 24	15	1.54 ± 0.16	0.26 ± 0.05	1.58 (30)	0.17 ± 0.01	0.51 ± 0.03
8 (outer head)	72.6	544 ± 25	12	2.61 ± 0.15	0.69 ± 0.12	1.24 (35)	0.23 ± 0.03	0.78 ± 0.18
Entire X-ray tail	530.9	22490 ± 150	75	2.09 ± 0.02	16.2 ± 0.03	0.98 (242)	6.78 ± 0.07	20.50 ± 0.02

Best-fit spectral parameters for an absorbed PL model for the contour regions shown in Figure 4. N_{H} was fixed at $2.7 \times 10^{22} \text{ cm}^{-2}$. The unabsorbed flux $F_{X,-12}$ and luminosity $L_{X,33}$ are given in units of $10^{-12} \text{ erg cm}^{-2} \text{ s}^{-1}$ and $10^{33} \text{ erg s}^{-1}$, respectively, in the 0.5–8 keV range. The luminosity is calculated for a distance of 5 kpc. \mathcal{N}_{-4} is the PL model normalization in units of $10^{-4} \text{ photons s}^{-1} \text{ cm}^{-2} \text{ keV}^{-1}$ at 1 keV, and counts per bin refers to the number of counts in each energy bin.

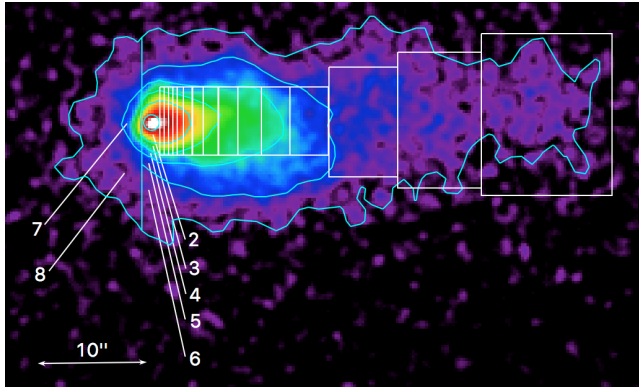


Figure 4. Merged ACIS counts image (the same as in the left panel of Figure 1) showing the regions used for spectral analysis (see Section 3.3 for details) – the boxes (white) and the numbered contour regions (cyan): Contour 2 (the red-colored area in the vicinity of the pulsar), Contour 3 (yellow area), Contour 4 (green area), Contour 5 (light blue and blue area), and Contour 6 (blue and purple area); Contours 7 (predominantly light blue) and 8 (purple) cover the area ahead of the pulsar.

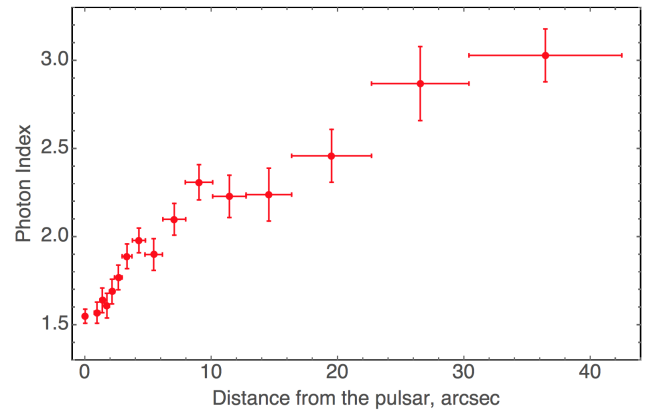


Figure 5. Photon index Γ as a function of distance from the pulsar. The points show the spectra extracted from the rectangular regions shown in Figure 4, with the left-most point corresponding to the pulsar. The horizontal error bars show the spatial extent (the width of each rectangle in the direction along the tail) of the regions from which the spectra were extracted, and the vertical error bars show 1σ uncertainties in the spectral slope Γ .

for each region to create an adaptively-binned spectral

map (Figure 6, bottom panel). The spectral map clearly

shows the spectral softening in front of and behind the pulsar (see above) as well as some hints of lateral softening.

3.3. HRC Timing

To search for X-ray pulsations, we performed the Z_n^2 ($n = 1, 2$) periodicity search (Buccheri et al. 1983) in the archival HRC data (ObsID 9106). Prior to searching, we corrected the event arrival times from the pipeline-produced Level 2 event list to the solar system barycenter using the CIAO task `axbary`. We restricted the search to $N = 350$ events located within $r = 0''.4$ centered on the brightest pixel of the HRC image of the Mouse PWN. The choice of the region size was dictated by the distance up to which the PWN core maintains an approximately round shape consistent with that of a point source.

The observation time span, $T_{\text{span}} = 57,760$ s, provides $\sim 1/T_{\text{span}} = 17.3$ μHz resolution. There is a known wiring error with the HRC-I detector which causes the photon arrival times to be associated with that of the following event, which may or may not have been telemetered, thus degrading the timing accuracy to roughly the mean time between events⁷. Since there were 3,627,988 total counts recorded by the entire detector during the 57.76 ks observation, the source photon arrival times are expected to be off by 15.92 ms on average. This should further degrade the resolution by broadening Z_n^2 peaks.

We found the maximum values $Z_1^2 = 3.0$ and $Z_2^2 = 6.8$ in the ± 18 μHz range around the expected $\nu = 10.1190144683(5)$ Hz (at MJD 54503.9) based on the *Fermi* LAT ephemeris⁸. We chose to search over a frequency range that is wider than the uncertainty of the predicted frequency because the pulsar is known to exhibit glitches according to the the *Fermi* LAT ephemeris. We note that the epoch of the HRC observation is outside the validity ranges of both the Fermi LAT (MJD 54634.203–54941.497) and ATNF (MJD 52306–52918) ephemerides. We picked the Fermi LAT ephemeris for the frequency prediction because it is closest to the HRC observation date. Using the more distant ATNF ephemeris results in the predicted frequency of 10.119000323(2) Hz which is 14.1 μHz away from the Fermi LAT ephemeris prediction.

We estimated the upper limit on the observed pulsed fraction p_{obs} at 99.73% confidence (3σ) by solving Equation (8) of Fierro et al. (1995) and found $p_{\text{obs}} < 34\%$. However, the intrinsic pulsed fraction limit could be higher due to the presence of high background contamination from the surrounding nebula. From the surface brightness of the nebula in the immediate vicinity of the pulsar, we estimate that out of the $N_{\text{tot}} = 350$ counts extracted from the region centered on the pulsar, roughly half of the counts ($N_{\text{bkg}} = 170$) come from the nebula. Thus, the upper limit on the intrinsic pulsed fraction could be as high as $p_{\text{int}} = p_{\text{obs}}(1 + N_{\text{bkg}}/N_{\text{tot}}) = 51\%$.

4. DISCUSSION

The new deeper *Chandra* observations of the Mouse PWN have allowed us to better characterize its spatial

and spectral morphology. Together with the multiwavelength data described below, they provide additional constraints on the PWN parameters and on the pulsar magnetosphere geometry.

4.1. Linking Compact PWN Morphology with Magnetosphere Geometry

Pulsars which share similar pulse profiles in both radio and γ -rays are likely to have similar viewing angles ζ (between the line of sight and pulsar spin axis) and similar magnetic inclination angles α (between the spin and magnetic dipole axes), as current models of magnetospheric emission suggest that the observed pulse profile shapes are primarily determined by α and ζ (see, e.g., Muslimov & Harding 2004). Radio and γ -ray pulse profiles have been used to infer α and ζ for different magnetosphere models (e.g., Romani & Watters 2010; Pierbattista et al. 2016).

Before it is affected by interaction with the external medium, the initially-axisymmetric wind flow causes the compact PWN appearance change with ζ while the latitudinal properties of the wind are expected to depend on α (Bühler & Giomi 2016). Therefore, one might expect that PWNe powered by pulsars with similar ζ and α will resemble each other; i.e., there will be a correlation between the PWN morphologies and the pulse profiles of pulsars powering these PWNe. However, the differing magnitudes and directions of pulsar velocities (characterized by angle θ between \vec{v} and the spin axis) can have a significant impact on the PWN morphologies resulting in different PWN appearances even when ζ and α are similar. This is particularly important for supersonically moving pulsars (see Kargaltsev et al. 2017). For example, PSRs J1509–5058 and J1709–4429 (B1706–44) have remarkably similar pulse profiles (see Figure 8; middle and bottom panels). The similarities include the separations between the radio and γ -ray peaks, the double-peaked morphologies, as well as the widths of the γ -ray pulses and the relative strength and the separation between the two γ -ray peaks. Although the X-ray PWNe of these two pulsars appear to be quite different at first glance, the similarities can be identified after accounting for differences in the pulsar velocities. According to Romani et al. (2005), the transverse velocity of PSR J1709–4429 (B1706–44) is $\lesssim 40$ km s $^{-1}$ while for PSR J1509–5058 the velocity is substantially larger, 160–640 km s $^{-1}$ (Klingler et al. 2016a). The larger velocity can explain the more curved jets and much more collimated extended tail of PSR J1509–5058 (see Klingler et al. 2016a). Yet, in both cases one can see two jets of roughly-equivalent brightness (implying a large ζ) and relatively dim tori compared to the jets (suggesting that α is not substantially large). In fact, for PSR J1709–4429, $\zeta = 53 \pm 0.4^\circ$ was measured by Romani et al. (2005) by fitting a Doppler-boosted torus model to the *Chandra* ACIS image of the compact PWN.

The radio and γ -ray light curves of the Mouse pulsar (J1747–2958) also share similarities with those of PSRs J1509–5850 and J1709–4429 (see Figure 8). Here, the only differences are that the Mouse’s γ -ray pulse profile is slightly wider (with a deeper trough) and more asymmetric compared to those of J1509 and J1709 (see Figure 8). In radio, all three pulsars display single peaks

⁷ see <http://cxc.harvard.edu/cdo/hrc/timing.html> for details.

⁸ https://fermi.gsfc.nasa.gov/ssc/data/access/lat/ephems/lat_psrcat/radio/ephem_J1747-2958_gbt.par

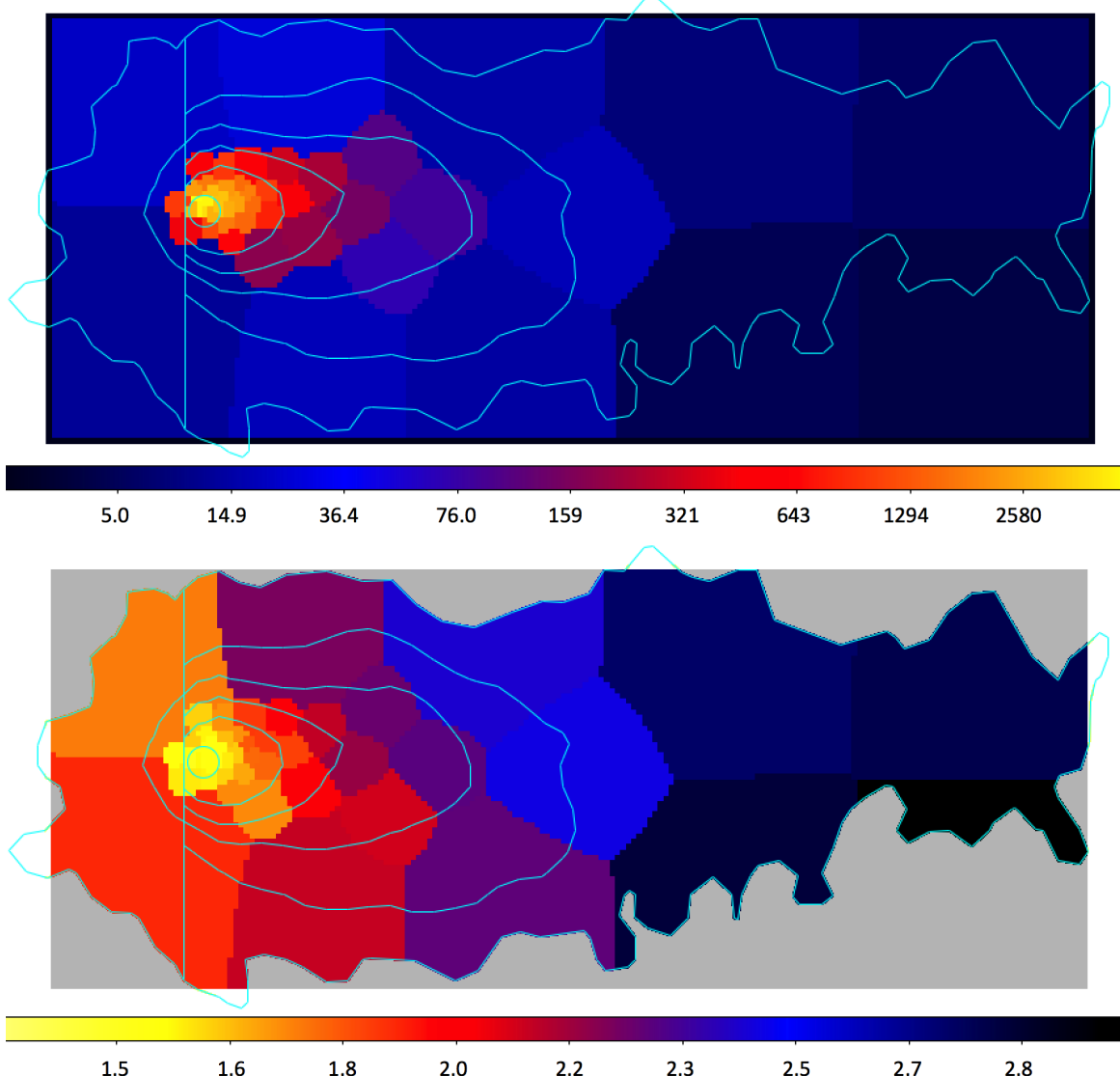


Figure 6. Top: Adaptively-binned merged image of the Mouse PWN (see Section 2). The color bar shows brightness in units of counts arcsec^{-2} . Bottom: Adaptively-binned spectral map of the Mouse PWN. The color bar shows the photon index. The cyan brightness contours (the same as in Figure 4) are overlaid, and the areas outside of them are grayed out for illustrative purposes.

with very similar phase separation from the γ -ray pulses. According to the Outer Gap magnetospheric emission model (e.g., Romani & Watters 2010), this implies a fairly large ζ and a similarly large α (to ensure that both γ -ray and radio pulsations can be seen). The stronger asymmetry and a deeper minimum between the pulses can be attributed to a large α , $\alpha \sim 70^\circ - 90^\circ$, which is also a plausible range for ζ . It is likely that these angles are somewhat larger for J1747 than those of PSRs J1509 and J1709. Comparison of the J1747 γ -ray and radio pulse profiles with simulated pulse profiles using the Two Pole Caustic (TPC) and Outer Gap (OG) γ -ray emission models (see Figure 2 of Watters et al. 2009) suggest the plausible ranges of angles $\zeta_{\text{OG}} \sim 58^\circ - 78^\circ$, $\zeta_{\text{TPC}} \sim 40^\circ - 71^\circ$, $\alpha_{\text{OG}} \sim 47^\circ - 80^\circ$, and $\alpha_{\text{TPC}} \sim 39^\circ - 70^\circ$. These considerations help to interpret the appearance of the compact nebula discussed in the next section.

4.2. PWN Core and Pulsar

The peak of the X-ray brightness in the ACIS image of the compact PWN is within $0''.35$ (0.7 ACIS pixels) from the radio timing position of the pulsar (corrected to the epoch of the ACIS observation), which is within the range of typical offsets in the *Chandra* World Coordinate System⁹. In the HRC image, the shape of the brightness peak is coincident with a point source (see the right panel in Figure 1). This indicates that the unresolved X-ray emission (as seen in the ACIS images) may be coming from the pulsar at the heart of Mouse PWN. The spectrum of the PWN core extracted from an $r = 0''.74$ aperture (see Section 3.2.1) is nonthermal and can be described by an absorbed PL with $\Gamma = 1.55 \pm 0.04$. This slope is only slightly smaller than $\Gamma = 1.65 \pm 0.02$ obtained from the absorbed PL fit to the emission from the immediate vicinity of the pulsar (region 2 in Figure 4). Therefore, there is no spectral evidence for pulsar emis-

⁹ see <http://cxc.harvard.edu/cal/ASPECT/celmon/>

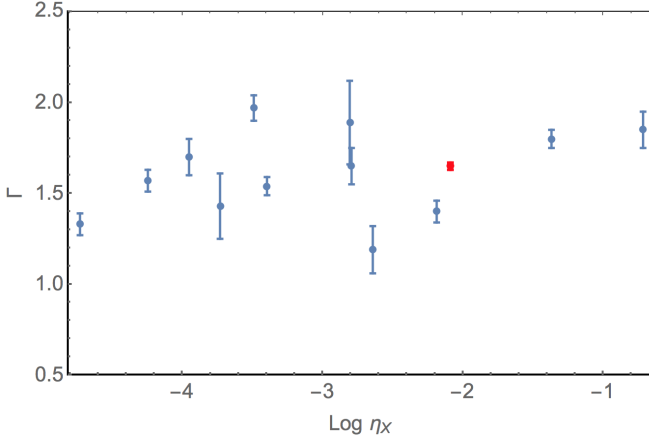


Figure 7. Slopes Γ of the X-ray spectra emitted by particles injected at the termination shock vs PWN X-ray (0.5–8 keV) efficiency η_X for the following PWNe (listed by increasing η_X): Vela, J1741-2054, B1951+32 (CTB 80), J1509-5850[†], 3C 58, B0355+54[†], G11.2-0.3, G54.1+0.3, B1509-58 (MSH 11-52), G21.5-0.9, Mouse (shown in red), Crab[†], and Kes 75. The Γ values for PWNe noted with [†] were taken from Klingler et al. (2016a,b) and Mori et al. (2004), and all others were obtained using the spatially-resolved spectral map procedure described above (see Kargaltsev et al. 2017 for the spectral maps). The distances and parameters used to obtain the efficiencies were taken from Kargaltsev & Pavlov (2010), and those for PSR J1741-2054 from Auchettl et al. (2015).

sion dominating the PWN emission in the core of the nebula. The flux extracted from the core region corresponds to an X-ray luminosity $L_{X,\text{psr}} = (5.83 \pm 0.09) \times 10^{33}$ erg s⁻¹ (in 0.5–8 keV, at $d = 5$ kpc), yielding an X-ray efficiency $\eta_X \equiv L_X / 4\pi d^2 = 2.3 \times 10^{-3}$. The core luminosity is a factor of 3.5 smaller than the luminosity of the entire PWN (excluding the pulsar) in X-rays, $L_{X,\text{pwn}} = (2.05 \pm 0.02) \times 10^{34}$ erg s⁻¹, with $\eta_X = 8.2 \times 10^{-3}$. In Figure 7 we compare η_X and the spectral slopes of the X-ray spectra emitted by particles injected at the termination shock with those of other X-ray-bright PWNe. Assuming uncooled spectra (which is likely to hold in the vicinity of the pulsar), the observed spectral slopes, $1 < \Gamma < 2$, correspond to slopes $1 < p < 3$ ($p \equiv 2\Gamma - 1$) of the particle SED, $dN/dE_e \propto E_e^{-p}$ (for the Mouse, $p = 2.3$).

4.3. Compact Nebula and Tail

Hales et al. (2009) measured the transverse velocity of the Mouse PWN, $v_\perp = (306 \pm 43)d_5$ km s⁻¹. Together with the HRC image this measurement allows us to estimate the Mach number for the pulsar. The HRC image (Figure 1, right panel) shows extended emission at the apparent apex of the PWN, resolved from the core, which is seen for up to $\simeq 1''$ ahead of the pulsar. This corresponds to the projected distance $r_{\perp,s} = 7.5 \times 10^{16}d_5$ cm. At this distance, the pulsar wind pressure, $P_w = \dot{E}f_\Omega(4\pi c r_s^2)^{-1} = 1.2 \times 10^{-9}f_\Omega d_5^{-2}$ dyn cm⁻² (f_Ω takes into account PW anisotropy; $f_\Omega = 1$ for isotropic wind), is balanced by the sum of the ambient pressure, $P_{\text{amb}} = \rho k T (\mu m_H)^{-1} = 1.38 \times 10^{-12} n T_4$ dyn cm⁻², and the ram pressure, $P_{\text{ram}} = \rho v^2 = 1.67 \times 10^{-10} n v_7^2 = 1.67 \times 10^{-10} n v_{\perp,7}^2 \sin^{-2} i$ dyn cm⁻². Here $T_4 = T/10^4$ K is the ISM temperature, $v_7 = v/10^7$ cm s⁻¹ is the 3D pul-

sar velocity, i is the angle between the line of sight and the pulsar motion direction, μ is the ISM mean molecular weight¹⁰, and $n = \rho/(\mu m_H)$ is the ISM number density in units of cm⁻³. Assuming $P_{\text{ram}} \gg P_{\text{amb}}$ (or $\mathcal{M} \gg 1$), we estimated the ambient ISM number density as $n \simeq 0.8 f_\Omega \sin^2 i$ cm⁻³ (if the velocity vector is close to the plane of sky, the shape of the bow shock in the vicinity of the apex can be approximated by a sphere resulting in $r_s = r_{\perp,s}$). The above estimate of the number density suggests a warm or hot ISM phase with the sound speed $c_{\text{ISM}} \simeq 10 - 100$ km s⁻¹ (see Section 21.1.2 of Cox 2000), unless $f_\Omega \gg 1$. We can also estimate the Mach number $\mathcal{M} = (P_{\text{ram}}/\gamma_a P_{\text{amb}})^{1/2} = v/c_{\text{ISM}} \simeq$, which typically ranges from a few to ~ 30 (here $\gamma_a = 5/3$ is the ISM adiabatic index). Very low values of \mathcal{M} (i.e., $\mathcal{M} \sim 1$) are not likely as it would be difficult to explain the presence of the very long collimated radio tail.

In radio, the PWN behind the pulsar appears to expand laterally up to $\sim 1.5'$ from the pulsar, while the X-ray PWN behaves quite differently: it steadily narrows beyond $\simeq 15''$ downstream from the pulsar (see Figures 1 & 3). The narrowing of the X-ray PWN could be explained by the more efficient cooling of X-ray emitting electrons located further from the tail's axis caused by either a substantially slower flow velocity compared to the inner channel of the tail, or by a stronger magnetic field. The latter is not likely because the higher magnetic field would enhance the synchrotron emission brightness in radio and in X-rays further from the tail's axis, which is not seen (unless the electron density is lower there). On the other hand, the former interpretation contradicts to the results of numerical simulations (see Figure 1 of Bucciantini et al. 2005) which suggest that the flow is slower in the inner channel behind the pulsar. This, however, may be the result of limitations in the model setup. The lower energy radio-emitting electrons have much longer cooling timescales and therefore their appearance in the images is not affected across distances on the order of the size of the X-ray nebula.

In the X-ray images, the Mouse CN displays a “filled” morphology similar to those of the X-ray CNe around the supersonic B0355+54 (Klingler et al. 2016b) and J1741-2054 (Auchettl et al. 2016) pulsars. Such a morphology is contrast to the “hollow” morphologies of the X-ray CNe of Geminga (Posselt et al. 2017) and J1509-5850 (Klingler et al. 2016a), which are also moving supersonically. A somewhat abrupt decrease in brightness occurring $\simeq 10''-15''$ behind the pulsar is shown by the dashed line in Figure 1 (left panel). The drop in surface brightness is also seen in the VLA 1.5 GHz image, at the same position and angle as seen in the X-rays. A similarly abrupt drop in brightness occurs in the B0355+54 CN at a comparable distance behind the pulsar (Klingler et al. 2016b; see Figure 9, top right panel). However, in the B0355 CN, which appears to be symmetric with respect to the pulsar's motion trajectory, the drop occurs along a line perpendicular to the motion direction. For the Mouse CN, this line is inclined substantially with respect to the Mouse pulsar velocity direction (see Figure 9, top left panel). If this line corresponds to the edge of a flattened structure (e.g., an abrupt change in the

¹⁰ We assume solar abundances, $\mu = 1.37$, in all estimates.

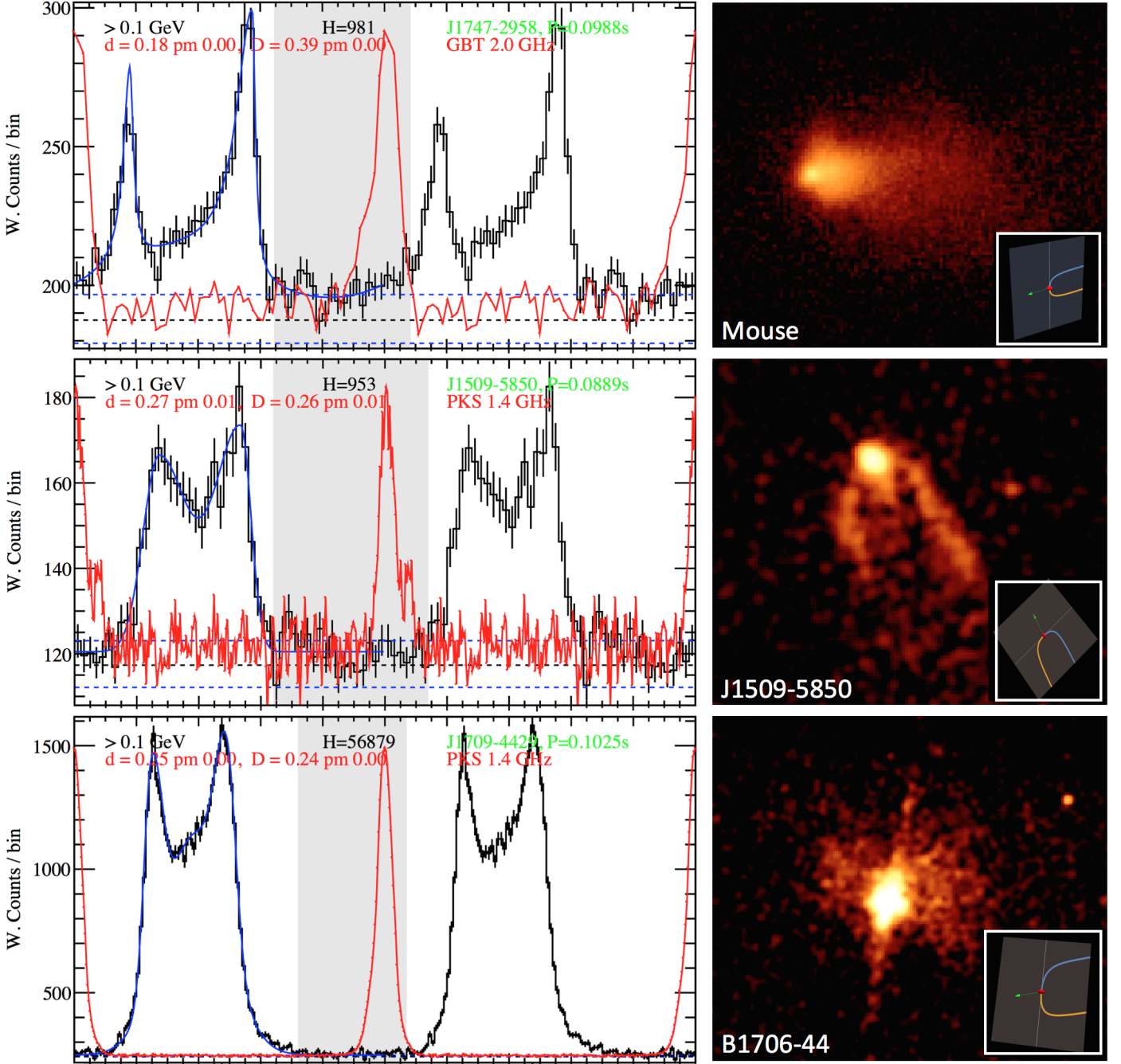


Figure 8. Radio and γ -ray pulse profiles of the Mouse (top), J1509–5850 (middle), and J1709–4429 (B1706–44, bottom) pulsars, and *Chandra* ACIS images of their PWNe. The insets in the X-ray images are the schematic illustrations of the probable orientations of the spin axis, with the jets (initially launched along the spin axis) bent by the ram pressure due to pulsar motion (the motion direction is shown by green arrows). The pulse profiles taken from the 2nd *Fermi* LAT pulsar catalog (Abdo et al. 2013) show the weighted counts per bin as a function of rotational phase (2 periods are shown), and the H-test value H . The letters d and D represent the lag of the first γ -ray peak relative to the radio fiducial phase, and the separation of the outermost γ -ray peaks, respectively (see Section 5.1 and Appendix A of Abdo et al. 2013 for details).

properties of an equatorial outflow deformed by the ram pressure), then it would imply that part of the Mouse's velocity vector is pointing out of the plane of the sky toward the observer, while the equatorial plane is oriented at a large angle from the plane of the sky (Figure 9, top left inset), with the viewing angle $\zeta \sim 70^\circ$ from the pulsar spin axis. The B0355+54 CN appearance can be explained by a similar equatorial outflow if

the pulsar's velocity vector is perpendicular to the line-of-sight and the equatorial plane is close to the plane of the sky (Figure 9, top right inset). The above interpretation of the Mouse PWN (i.e., the velocity vector is nearly perpendicular to the spin axis) is compatible with the viewing geometry suggested by the γ -ray light curve modeling discussed above, which also indicates that our line of sight is oriented near the equatorial plane (see

Section 4.1). Since radio pulsations are seen, this also suggests that the pulsar's magnetic axis is significantly offset from its spin axis ($\alpha \sim 70^\circ$). The similarities of the Mouse's radio and γ -ray light curves with those of J1509 and J1707 suggest that the magnetic inclination angles of J1509 and B1706 are similarly large, and also have similar viewing angles.

Despite the above-discussed similarities between the CNs of the Mouse and B0355, the extended tails of these two pulsars show noticeable differences. The B0355 PWN spectra show no signs of spectral softening between the CN and its long X-ray tail, nor along the tail up to distances ~ 2 pc, while the Mouse PWN shows clear evidence of fast softening on scales < 0.1 pc (see Figure 5). The differences could be explained if the Mouse tail has either a much higher magnetic field strength or a much slower bulk flow velocity. The latter seems to be difficult to reconcile with the extremely long (36 pc) collimated radio tail (see Figure 1 in Yusef-Zadeh & Gaensler 2005), so the former interpretation is more likely unless there is substantial re-acceleration of the flow at large distances from the pulsar in the Mouse's tail or if some “re-heating” mechanism operates in the tail of B0355 which does not operate in the Mouse tail (e.g., the flow is much more turbulent in the B0355 tail). In addition, the B0355 tail is far less collimated compared to that of the Mouse, which may explain why it is not seen in radio (Ng et al. in prep.). The reduced collimation is likely the consequence of a lower pulsar velocity. Finally, the 4.89 GHz VLA image of the Mouse tail (Figure 3, top right panel) shows hints of regular “ripples” in the narrow part of the radio tail at $\gtrsim 2.5$ from the pulsar. Unless the ripples are due to instrumental artifacts¹¹, they may reflect the structure of magnetic field in the tail (e.g., magnetic field enhancements possibly associated with multiple Mach disks; see Morlino et al. 2015).

4.4. Multi-Wavelength Spectrum

The Mouse has been previously observed with the VLA between 1.5 and 15 GHz (Camilo et al. 2002; Yusef-Zadeh & Gaensler 2005; Hales et al. 2009) and has been identified in a 330 MHz VLA observation (Hyman et al. 2005). We have also investigated the 150 MHz GMRT pipeline-produced image from the TIFR GMRT Sky Survey (TGSS; Intema et al. 2017) and the Spitzer image from the 24 μ m MIPS Galactic Plane Survey (Gutermuth & Heyer 2015), which are shown in Figure 10. In both cases we found extended objects positionally coincident with the Mouse CN. In the low-resolution GMRT image (Figure 10, left panel) the source has an elongated shape consistent with the extent of the X-ray tail. In the much higher resolution 24 μ m image most of the emission comes from the vicinity of pulsar position (associated with the source MG359.3052–00.8412; Gutermuth & Heyer 2015) while the fainter extended emission could be due to unrelated foreground/background emission because it does not conform well the shape of the X-ray or radio tail. The lack of 2MASS counterpart hints that MG359.3052–00.8412, with a 24 μ m flux of 17.7 ± 2.1 mJy, may be associated with the Mouse

¹¹ In radio interferometer images, a ripple pattern often surrounds bright sources and can typically be seen in the faint background, which is not the case here.

PWN head. However, even in this case, it might not be associated with the pulsar wind synchrotron emission¹². High-resolution IR observations are needed to establish the nature of MG359.3052–00.8412 and its connection to the Mouse PWN.

The radio and X-ray measurements (obtained using the X-ray tail region shown in the left panel of Figure 3) suggest that the multiwavelength spectrum from this region (see Figure 11) should experience at least one break between $\sim 10^{-5}$ eV (~ 2 GHz) and 500 eV if the spectrum can be approximated by PLs (see Figure 11).

If a single break (around 10^{-2} eV) is assumed (illustrated by the gray line in Figure 11), then the low-frequency radio spectrum can be fitted¹³ by a PL with $\Gamma_R = 1.07 \pm 0.05$ with a low-frequency (150 MHz to 0.01 eV) luminosity of $(7.9 \pm 3.4) \times 10^{31}$ erg s $^{-1}$ and a high-frequency (0.01 eV to 100 keV) luminosity of $(5.6 \pm 0.6) \times 10^{35}$ erg s $^{-1}$ for the X-ray tail region. The magnitude of the spectral break between the radio and X-ray spectra¹⁴ corresponds to $\Delta\Gamma \approx 1.0 \pm 0.1$. Although large (>0.5) values of $\Delta\Gamma$ between the radio and X-ray spectra are common for PWNe (e.g., Chevalier 2005, Reynolds et al. 2017), they are challenging to obtain from standard synchrotron cooling considerations unless additional mechanisms, such as entrainment, turbulent magnetic field amplification, diffusion, and/or reconnection are invoked. Modeling these processes is beyond the scope of our paper; below we briefly discuss synchrotron cooling scenarios and the physical constraints they impose.

Although the existing data are consistent with a single break in the PL spectrum, a double break (or a more complex behavior) is not excluded. In fact, one would expect to see a double break if the lower boundary energy of the injection spectrum is large enough (the origin of the spectral breaks is explained in the Appendix). If the injected electron SED is a single PL with a slope p and lower and upper boundary energies $\gamma_m m_e c^2$ and $\gamma_{\max} m_e c^2$, respectively, then the low-energy injection break in the photon spectrum would be at $h\nu_m \simeq 5 \times 10^{-6} (\gamma_m/1000)^2 (B/100\mu G)$ eV. On the other hand, we expect the cooling break energy, $h\nu_c \gtrsim 1.5 (t_r/1 \text{ kyr})^{-2} (B/100\mu G)^{-3}$ eV, where t_r is the residence time of the pulsar wind electrons in the X-ray tail region ($t_r = l_{\text{tail}}/v_{\text{flow}} \leq 0.1$ kyr for $v_{\text{flow}} \leq 10,000$ km s $^{-1}$, see below). Since γ_m is not known, the ordering of $h\nu_c$ and $h\nu_m$ is also not known. From here on we define conditions with $\nu_c < \nu_m$ as “globally fast cooling”, and $\nu_m < \nu_c$ as “globally slow cooling”. Possible spectra

¹² For instance, the Crab PWN spectrum has a bump in IR due to dust scattering (Atoyan & Aharonian 1996).

¹³ When fitting a PL to the radio fluxes, we weighted the values by the inverse of the corresponding fractional uncertainties. For the GMRT flux measurement, the extraction region size is comparable to the beam size, so we assume a 50% fractional uncertainty. For the VLA data, the precise values of uncertainties depend on the specifics of the data reduction pipeline parameters used and hence difficult to estimate. Since at 4.77 GHz two different array configurations lead to fluxes that differ by roughly 50%, we also conservatively ascribe a 50% uncertainty to all VLA flux measurements.

¹⁴ We note that although the spatially-averaged CXO spectrum extracted from the X-ray tail region fits a PL with $\Gamma_X = 2.09 \pm 0.03$, the spatially-resolved spectroscopy shows that the slope depends on distance from the pulsar (see Section 3.2.2).

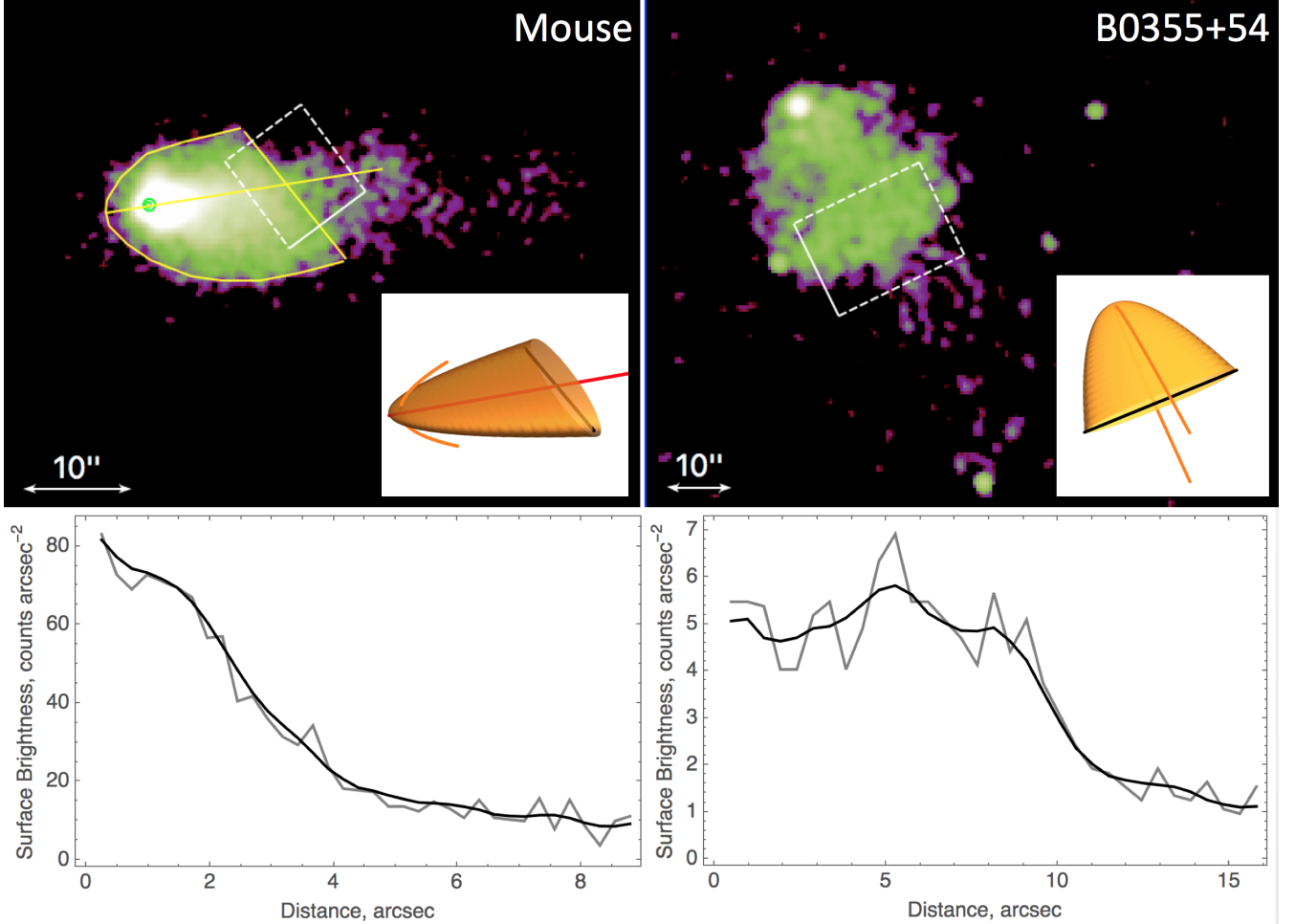


Figure 9. *Top Left:* Merged ACIS image of the Mouse CN, binned by a factor of 0.5, and smoothed with a 3-pixel ($r = 0''.74$) Gaussian kernel. The solid yellow contour outlines the outer edge of the putative deformed equatorial outflow (see Section 4.3 for discussion), and the yellow line passing through the pulsar and trailing edge of the CN shows the symmetry axis of the CN (assuming the CN resembles the 3D structure shown in the inset). Shown in the inset is a 3D illustration of pulsar wind flattened near the CN equatorial plane, viewed from the same angle as the Mouse ($\sim 20^\circ$ offset from the equatorial plane). The curved orange lines illustrate polar outflows (jets) bent back by the ram pressure. *Bottom Left:* Plot of the surface brightness of the downstream end of the CN, obtained from the region enclosed by the dashed white box shown in the top left image. The gray curve was obtained without smoothing applied, and the black curve was obtained with the smoothed image. *Top Right:* ACIS image of the B0355+54 CN (smoothed with an $r = 1''.48$ Gaussian kernel), which features a similar CN composed of a deformed equatorial outflow and a similar trailing edge, viewed from near the pulsar spin (i.e., jet) axis (see Klingler et al. 2016b), with a similar inset, shown for comparison. *Bottom Right:* The surface brightness profile for the B0355 CN plotted in the same manner.

with two breaks at the break energies roughly consistent with the above values are shown in Figure 11 (the red dashed-dotted line implies $h\nu_m < h\nu_c$ while the green dashed-dotted line implies $h\nu_c < h\nu_m$).

At a given observing frequency and a given ordering of ν_m and ν_c , the spectral slope can be determined from synchrotron theory (an explanation is provided in the Appendix; see also Sari et al. 1998 and Section 5 of Piran 2004). Since the X-ray spectrum is softening rapidly along the tail, it is reasonable to assume that the X-ray emission is produced by fast-cooling electrons with $\nu > \nu_c$ (even if the bulk of the electrons have lower energies and are slow-cooling). In this case one can relate the slope p of the injected particle SED to the X-ray photon index as $p = 2\Gamma - 2$, regardless of whether $\nu_m > \nu_c$ or vice versa. This leads to a more conventional $p \approx 2.2$ expected from acceleration in relativistic shocks (see e.g., Bykov et al. 2017 and references therein) compared to $p \approx 3.2$ which would follow from $p = 2\Gamma - 1$ for

a spectrum produced by slow cooling electrons. If the X-ray slope is produced by fast-cooling electrons (which is likely), the overall change in slope (from radio to X-rays) is $\Delta\Gamma = 0.77 \pm 0.05$ because the lower energy slope $\nu F_\nu \propto \nu^{4/3}$ regardless of whether $\nu_m > \nu_c$ or vice versa (assuming that self-absorption is not occurring in the observed frequencies; see below). This change is consistent with the existing measurements within their uncertainties and is somewhat smaller than $\Delta\Gamma \approx 1.0 \pm 0.1$ for a PL with a single break (see Figure 11). In order to firmly discriminate between the double break and single break PL scenarios, the Mouse PWN must be resolved at mm (with ALMA) and IR (with HST) wavelengths.

4.5. Magnetic Field, Energetics, and Flow Velocity

The spectra extracted from the X-ray tail can be used to estimate the magnetic field. For an electron population producing synchrotron emission with photon index $\Gamma = (p + 2)/2$, the magnetic field B for a given mag-

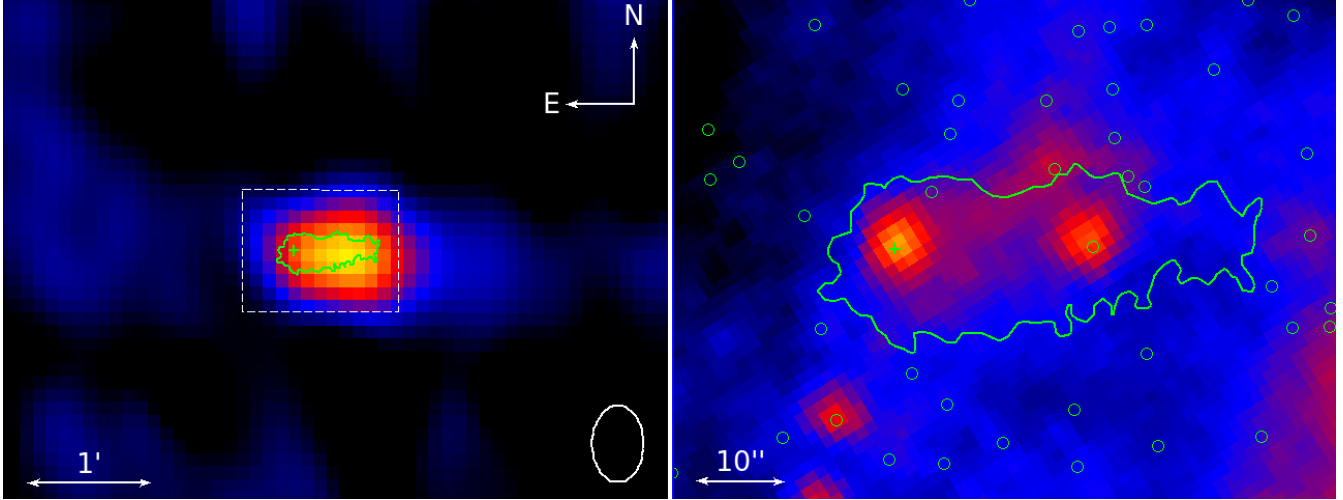


Figure 10. Left: GMRT 150 MHz image of the Mouse PWN. The white ellipse in the bottom right corner shows the synthesized beam size, and the dotted white box shows the field of view shown in the right panel. Right: *Spitzer* MIPS 24 micron image of the Mouse field, showing the head of the CN; the green circles mark nearby 2MASS point sources. In each of the panels the green cross marks the pulsar position, and the X-ray tail contour from Figure 3 is shown.

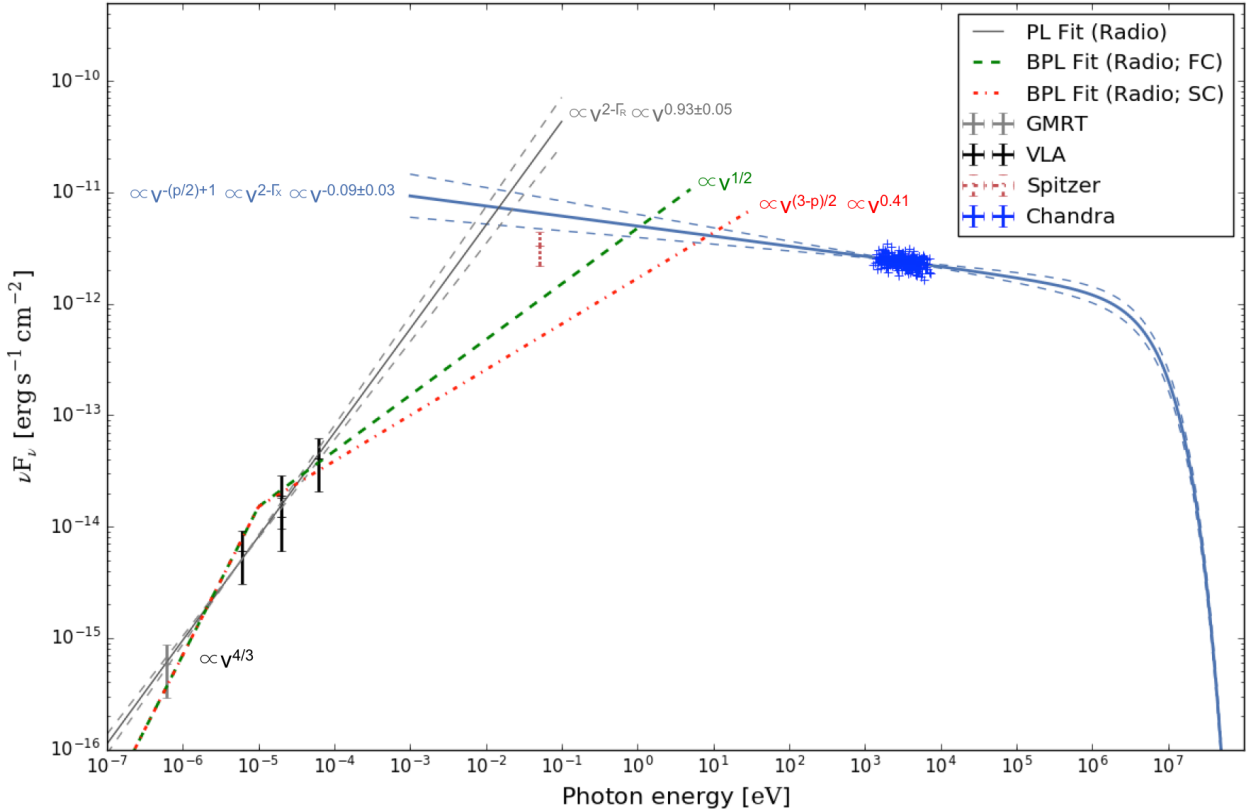


Figure 11. Multiwavelength spectrum of the X-ray tail region (the right section of the contour shown in Figure 3, left panel; this region excludes emission from the pulsar). The following data points are plotted: GMRT: 150 MHz; VLA: 1.47 GHz, 4.77 GHz (2 different array configurations), 14.9 GHz; *Spitzer*: 24 μ m; and the unabsorbed 1.2–8 keV *Chandra* fluxes (there were insufficient counts below 1.2 keV due to absorption). The high-energy synchrotron spectrum (blue lines) extrapolated from the *Chandra* data (blue points) was plotted with *naima* assuming a PL SED for the electrons with $p = 2\Gamma - 2 = 2.18$ (obtained from fitting the X-ray data). The exponential cutoff energy was set at 3.35 PeV, which is the maximum accelerating potential of the pulsar's polar cap, $\Phi = (3\dot{E}/2c)^{1/2}$; however, the spectrum is likely to exhibit an exponential cutoff at frequencies much lower than those corresponding to the maximum energy (as suggested by the observed rapid cooling), and hence this should be interpreted as an upper limit for the cutoff energy. The slope of the PL spectrum (blue lines) going through the X-ray data points is fixed by the fit to the X-ray spectrum ($\Gamma_X = 2.09 \pm 0.03$). The grey lines show a PL fitted to the radio data points ($\Gamma_R = 1.07 \pm 0.05$). Various spectral slopes corresponding to low-energy segments of PLs with double breaks correspond to different cooling regimes discussed in the text ($\nu_c < \nu_m$ – green; $\nu_m < \nu_c$ – red). The dashed lines represent 1σ uncertainties of the slopes.

netization parameter $\sigma = w_B/w_e$ (the ratio of magnetic field energy density to relativistic electron energy density) is related to the ratio of the synchrotron power P_{ν_1, ν_2} (i.e., luminosity; measured in the $\nu_1 < \nu < \nu_2$ frequency range) to the volume of the radiating particles V (see Section 2 of the Appendix for the derivation):

$$B \approx \left[\frac{\sigma(8\pi)^2}{V} \frac{(q_e m_e c)^{1/2} P_{\nu_1, \nu_2}}{\frac{4}{3}\sigma_T(2\pi\nu_c)^{1/2}} \right]^{2/7} \left(\frac{-\frac{\nu_c^{(-p+2)/2}}{-p+1} - \nu_m^{(-p+2)/2}}{\nu_2^{(-p+2)/2} - \nu_1^{(-p+2)/2}} \right) \quad (1)$$

for $\nu_m < \nu_c < \nu_1 < \nu_2$ (i.e., globally slow cooling), or

$$B \approx \left[\frac{\sigma(8\pi)^2}{V} \frac{(q_e m_e c)^{1/2} P_{\nu_1, \nu_2} (-p+2)}{\frac{4}{3}\sigma_T(2\pi)^{1/2} \nu_m^{(p-1)/2}} \right]^{2/7} \left(\frac{\log\left(\frac{\nu_m^{1/2}}{\nu_c^{1/2}}\right) - \frac{1}{-p+1}}{\nu_2^{(-p+2)/2} - \nu_1^{(-p+2)/2}} \right) \quad (2)$$

for $\nu_c < \nu_m < \nu_1 < \nu_2$ (i.e., globally fast cooling). For ν_1 and ν_2 we use the frequencies corresponding to 0.5 and 8 keV, the range over which P_{ν_1, ν_2} and $p = 2\Gamma - 2 = 2.18$ have been measured (see Table 3). As $P_{\nu_1, \nu_2} \propto d^2$ and $V \propto d^3$, the magnetic field estimate is not very sensitive to the assumed distance, $B \propto d^{-2/7}$. For a cylindrical X-ray tail with $r = 7''$ and length $l = 38''$ located at $d = 5$ kpc ($V \approx 2.4 \times 10^{54} \text{ cm}^3$)¹⁵, the magnetic field is in the range of $B \sim (200 - 250)\sigma^{2/7} \mu\text{G}$ for the globally slow cooling scenario and $B \sim (100 - 110)\sigma^{2/7} \mu\text{G}$ for the globally fast cooling scenario, for a plausible range of break energies. In the above estimates we use 7.25×10^{14} Hz (corresponding to 3 eV) and 2.4×10^9 Hz (see Figure 11) for ν_c and ν_m (interchangeably for the two scenarios).

At sufficiently low frequencies, the synchrotron spectrum becomes suppressed due to self-absorption. Assuming a known flux density $F_{\nu, \text{obs}}$ at some observed frequency ν_{obs} below ν_m and below ν_c , the spectrum becomes self-absorbed at a frequency ν_{SA} which can be estimated from (see e.g., Beniamini & Kumar 2016)

$$\frac{2\nu_{SA}^2}{c^2} \gamma(\nu_{SA}) m_e c^2 \frac{A}{4\pi d^2} = \left(\frac{\nu_{SA}}{\nu_{\text{obs}}} \right)^{1/3} F_{\nu, \text{obs}} \quad (3)$$

where $\gamma(\nu_{SA}) = (2\pi m_e c \nu_{SA} / q_e B)^{1/2}$ is the Lorentz factor of electrons radiating at ν_{SA} , and A is the emitting surface area¹⁶. We use the surface area of the assumed emitting cylindrical volume with radius $r = 7''$ and length $l = 38''$ described above. The specific values of the self-absorption frequency are not very sensitive to the exact choice of geometry (which would slightly change the estimate of surface area). For ν_{obs} and $F_{\nu, \text{obs}}$ we

¹⁵ Although the estimate of the volume is crude as it depends on the actual geometry of the flow (discussed in further detail below), the magnetic field estimate does not strongly depend on it, as $B \propto V^{-2/7}$.

¹⁶ Near the self-absorption frequency the flux scales with surface area instead of volume.

take the lowest available observed frequency (and corresponding flux) of 150 MHz because we see that, at least down to those frequencies, the spectrum has not been sufficiently steepened, so self-absorption must be below the observed range. We also choose a low enough ν_{obs} so that we can be sure that $F_{\nu, \text{obs}}$ scales as $\nu^{1/3}$ below that frequency (which holds for either the globally slow or globally fast cooling regimes at low enough frequencies). Solving Equation (3) we find $\nu_{SA} \simeq 60$ kHz. The self-absorption frequency is therefore expected to lie far below the observed range, and should not affect the observed spectrum. For illustrative purposes, even if we take ν_{obs} at 1.5 GHz (the lowest frequency observed with the VLA), the estimate of ν_{SA} changes by less than 20%. Thus, since we find ν_{SA} to be orders of magnitude below the observed range of frequencies, the choice of ν_{obs} (and $\nu F_{\nu, \text{obs}}$) is not a critical one.

Using the magnetic field estimates, we can estimate the average flow speed in the X-ray tail using the tail's energy transfer (injection) rate,

$$\dot{E}_{\text{Tail}} \sim (w + p) S v_{\text{flow}} \quad (4) \\ \sim 2.9 \times 10^{35} (B_{\text{eq}}/200 \mu\text{G})^2 (S/7.5 \times 10^{35} \text{ cm}^2) \\ \times (v_{\text{flow}}/1000 \text{ km s}^{-1}) [\sigma^{4/7} + (2/3)\sigma^{-3/7}]^2 \text{ erg s}^{-1},$$

and energy density

$$w = w_B + w_e = [B_{\text{eq}}^2/(8\pi)] (\sigma^{4/7} + \sigma^{-3/7})^2 \quad (5) \\ \sim 1.6 \times 10^{-9} (B_{\text{eq}}/200 \mu\text{G})^2 (\sigma^{4/7} + \sigma^{-3/7})^2 \text{ erg cm}^{-3}.$$

Here, v_{flow} is the average velocity of the flow passing through cross-sectional area S , w_B and w_e are the magnetic and particle energy densities, $w + p$ is the enthalpy density, $p = w_B + w_e/3$ is the pressure of the relativistic particles in the magnetic field, and B_{eq} is the equipartition magnetic field strength. When $\sigma = 3/4$, the term $(\sigma^{4/7} + \sigma^{-3/7})^2 \approx 3.92$ and is minimized. Equation (2) and the requirement that $\dot{E}_{\text{Tail}} < \dot{E}$ can be used to place constraints on v_{flow} . If the outflow is conical with a width of $13''$ in the bright CN ($S = 7.5 \times 10^{35} \text{ cm}^2$), then v_{flow} can not be much larger than $\approx 3,500 \text{ km s}^{-1}$ – a relatively low flow speed with which it would be difficult to explain the presence of the long collimated radio tail. However, if most of the X-ray tail is composed of a deformed equatorial outflow, then, at least initially, the tail may be best approximated as a flattened structure rather than a conical structure. This would reduce the cross-sectional area in Equation (4) and would allow higher flow speeds which are necessary to explain the long collimated tail seen in radio. For example, for an outflow $15''$ wide (the width of the CN at the brightness drop, see Figure 9) and $3''$ thick (a plausible estimate), the bulk flow velocity could be as high $\leq 10,000 \text{ km s}^{-1}$. More high-resolution observations at different wavelengths would allow one to more accurately discern the flow geometry and constrain the multiwavelength spectrum, the physical properties of the outflow, and the spectral breaks seen in the multiwavelength spectrum.

5. SUMMARY

We have analyzed the archival CXO ACIS and HRC observations, the new deep ACIS observations, and explored archival low-frequency data of the Mouse PWN.

The deep X-ray observations show that the Mouse PWN consists of a filled CN, followed by a $\sim 45''$ -long tail which narrows with distance from the pulsar. In radio, the nebula head expands in a conical fashion up to much larger distances ($\sim 1.5'$ behind the moving pulsar) and then forms a very long $\sim 10'$ collimated tail. In the HRC image we observe the projected bow shock apex $1''$ from the pulsar position.

The deep *Chandra* observations have produced a clearer picture of the PWN, which allows us to gain insight into the magnetic inclination and viewing angles of the pulsar when we also consider the geometry information encoded in the pulsar pulse profiles. The observed PWN morphology can be interpreted as an equatorial outflow deformed by the ram pressure and viewed from an angle $\sim 20^\circ$ offset from the equatorial plane, while the pulsar 3D velocity vector is turned out of the plane of sky toward the observer by a similar (small) angle. From the presence of the radio pulsations, we can infer that the magnetic axis of the pulsar is inclined by $\alpha \gtrsim 70^\circ$ from its spin axis, with our line of sight inclined from the spin axis by about the same angle ζ .

We find that the spectrum extracted from the pulsar region is well fit by an absorbed PL model with $\Gamma = 1.55 \pm 0.04$ and $N_H = 2.7 \times 10^{22} \text{ cm}^{-2}$, although this spectrum is most likely contaminated by the bright surrounding nebular emission or even dominated by this emission. The spectrum of the PWN softens with increasing distance from the pulsar, ranging from $\Gamma = 1.65 \pm 0.02$ in the inner regions to $\Gamma \approx 3.0 \pm 0.2$ at the end of the X-ray tail. These changes can be attributed to rapid synchrotron cooling in a strong magnetic field.

We have produced an adaptively-binned spectral map of the PWN to visualize the spectrum and the cooling trend. We also found that, despite the rapid spectral softening, the spatially-averaged X-ray spectrum of the entire X-ray PWN (excluding the pulsar) can be well-fit by a single absorbed PL with $\Gamma_X = 2.09 \pm 0.02$ (this highlights the problem with inferring the spectrum of particles injected at the termination shock from the spatially-averaged spectra of large regions). At a distance of 5 kpc, the PWN exhibits an $0.5\text{--}8 \text{ keV}$ luminosity $L_X = (2.05 \pm 0.02) \times 10^{34} \text{ erg s}^{-1}$, yielding a relatively high X-ray efficiency of the PWN, $\eta_X \approx 0.008$.

We have identified the Mouse PWN in the 150 MHz image from the TIFR GMRT Sky Survey. We performed an assessment of the multiwavelength spectrum of the X-ray tail using the GMRT and VLA data and found that the shape of the spectrum between 150 MHz and 8 keV can be approximated by a broken PL with at least one break between $2.4 \times 10^9 \text{ Hz}$ (10^{-5} eV) and $1.2 \times 10^{17} \text{ Hz}$ (0.5 keV). Using the multiwavelength data we estimated the equipartition magnetic field in the X-ray tail $B \sim 100\text{--}200 \mu\text{G}$, which is consistent with the rapid synchrotron cooling observed.

Facilities: CXO (ACIS, HRC), VLA, GMRT, Spitzer

Support for this work was provided by the National Aeronautics and Space Administration through *Chandra* Award Number G03-14082 issued by the *Chandra* X-ray Observatory Center, which is operated by the Smithsonian Astrophysical Observatory for and on behalf of the National Aeronautics and Space Administration un-

der contract NAS8-03060. C.-Y. N. is supported by a GRF grant from the Hong Kong Government under HKU 17305416P.

APPENDIX

EXPECTED SPECTRAL BREAKS

In this section we briefly explain the origin of the spectral breaks for the fast and slow cooling scenarios, as described in Section 5 of Piran (2004). The characteristic synchrotron photon energy (in the observer frame) emitted by a relativistic electron with Lorentz factor γ in magnetic field B is

$$h\nu_{\text{syn}} = \frac{\hbar q_e B}{m_e c} \gamma^2 \quad (\text{A1})$$

where q_e is the electron charge. The power emitted by such an electron is

$$P_{\text{syn}} = \frac{4}{3} \sigma_T c \frac{B^2}{8\pi} \gamma^2 \quad (\text{A2})$$

where σ_T is the Thompson cross-section. The instantaneous synchrotron spectrum emitted by the electron is approximately a PL with $F_\nu \propto \nu^{1/3}$ up to the characteristic frequency ν_{syn} , above which it exponentially decays. The peak power (emitted at ν_{syn}) is

$$P_{\nu,\text{max}} \approx \frac{P(\gamma)}{\nu_{\text{syn}}} = \frac{\gamma m_e c^2 \sigma_T}{3q_e} B. \quad (\text{A3})$$

Energetic electrons will cool rapidly until they reach γ_c , the Lorentz factor of electrons that have cooled on a hydrodynamic time scale (i.e., the travel time of an electron traversing the X-ray tail region from which we extracted the spectrum). So for an electron with initial Lorentz factor γ_i , the time-integrated spectrum is $F_\nu \propto \nu^{-1/2}$ for $\nu_{\text{syn}}(\gamma_c) < \nu < \nu_{\text{syn}}(\gamma_i)$.

The spectrum of the electron population (prior to cooling) can be obtained by integrating over the electrons' initial SED, which can be described by a PL with index p : $N(\gamma) \propto \gamma^{-p}$ for $\gamma_m < \gamma < \gamma_{\text{max}}$. The low-energy part of the spectrum (above the synchrotron self-absorption frequency ν_{SA} , and below both ν_m and ν_c) will be the sum of the contributions of the electrons' low-frequency emission, so $F_\nu \propto \nu^{1/3}$, independent of the electron SED and characteristic of synchrotron emission. The higher-energy electrons (i.e., those radiating above both ν_m and ν_c) will cool rapidly and emit most of their energy $\gamma m_e c^2$ at their synchrotron frequency. The number of electrons with Lorentz factor γ is $\propto \gamma^{-p+1}$, and their energy is $\propto \gamma^{-p+2}$. When these electrons cool, most of their energy is radiated at $\sim \nu_{\text{syn}}(\gamma) \propto \gamma^2$, and thus $F_\nu \propto \gamma^{-p} \propto \nu^{-p/2}$.

In the intermediate-energy regime, the spectrum can either be globally slow cooling if typical electrons (with γ_m) do not cool on the hydrodynamic (HD) time scale, or globally fast cooling if they do. This is determined by γ_c , the Lorentz factor of an electron that does cool on an HD time scale t_{hyd} .

$$\gamma_c = \frac{3m_e c}{4\sigma_T (B^2/8\pi) t_{\text{hyd}}} \quad (\text{A4})$$

In the globally fast cooling case ($\gamma_c < \gamma_m$) typical electrons rapidly cool, and $\nu_c < \nu_m$. The low-energy part of the spectrum $F_\nu \propto \nu^{1/3}$ below ν_c . All cooling electrons are radiating between ν_c and ν_m . As the electron energy $\propto \gamma$ and typical frequency $\propto \gamma^2$, $F_\nu \propto \gamma^{-1} \propto \nu^{-1/2}$. Therefore,

$$F_\nu \propto \begin{cases} (\nu/\nu_c)^{1/3}, & \nu < \nu_c \\ (\nu/\nu_c)^{-1/2}, & \nu_c < \nu < \nu_m \\ (\nu_m/\nu_c)^{-1/2}(\nu/\nu_m)^{-p/2}, & \nu_m < \nu. \end{cases} \quad (\text{A5})$$

In this case, the peak energy emitted is at ν_m (in νF_ν).

In the globally slow cooling scenario ($\gamma_c > \gamma_m$), the majority of the electron population (with $\gamma \sim \gamma_m$) is not cooling efficiently. At the low-energy end of the spectrum $F_\nu \propto \nu^{1/3}$ below ν_m , and $F_\nu \propto \nu^{-p/2}$ above ν_c at the high-energy end. In the intermediate region, $F_\nu = N[\gamma(\nu)]P[\gamma(\nu)]d\gamma/d\nu \propto \nu^{-(p-1)/2}$. Thus,

$$F_\nu \propto \begin{cases} (\nu/\nu_m)^{1/3}, & \nu < \nu_m \\ (\nu/\nu_m)^{-(p-1)/2}, & \nu_m < \nu < \nu_c \\ (\nu_c/\nu_m)^{-(p-1)/2}(\nu/\nu_c)^{-p/2}, & \nu_c < \nu. \end{cases} \quad (\text{A6})$$

Here, the peak flux occurs at ν_m , but the peak energy is emitted at ν_c (assuming $p > 2$). For further detail, see Section 5 of Piran (2004). The observed spectral slopes can vary from the predicted values if turbulent magnetic reconnection is occurring in the emitting region (see, e.g., Xu et al. 2017).

EQUIPARTITION MAGNETIC FIELD

If the majority of the electron population is globally slow cooling, the SED can be described by

$$\frac{dN}{d\gamma} = \begin{cases} A\gamma^{-p}, & \gamma_m < \gamma < \gamma_c \\ A\gamma_c\gamma^{-p-1}, & \gamma_c < \gamma < \gamma_{\max} \end{cases} \quad (\text{B1})$$

for some normalization A , and maximum Lorentz factor γ_{\max} . We assume $\nu_m < \nu_c < \nu_1 < \nu_2$ (and the same ordering for the Lorentz factors of electrons corresponding to each frequency), and that the flux is measured in the range $\nu_1 < \nu < \nu_2$ (in our case, this corresponds to the 0.5–8 keV). The synchrotron power in this range (i.e., the luminosity measured between ν_1 and ν_2) is

$$\begin{aligned} P_{\nu_1, \nu_2} &= \int_{\nu_1}^{\nu_2} \frac{dN}{d\gamma} c \frac{4}{3} \sigma_T \gamma^2 \frac{B^2}{8\pi} d\gamma \\ &= A\gamma_c \frac{4}{3} \sigma_T c \frac{B^2}{8\pi} \left(\frac{\gamma_2^{-p+2} - \gamma_1^{-p+2}}{-p+2} \right) \end{aligned} \quad (\text{B2})$$

where γ_1, γ_2 are the Lorentz factors of electrons radiating at ν_1, ν_2 correspondingly. The normalization A is related to the total energy in the electrons E_e :

$$\begin{aligned} E_e &= \int_{\gamma_m}^{\gamma_{\max}} \frac{dN}{d\gamma} \gamma m_e c^2 d\gamma \\ &= A m_e c^2 \left[\frac{\gamma_c^{-p+2} - \gamma_m^{-p+2}}{-p+2} + \gamma_c \left(\frac{\gamma_{\max}^{-p+1} - \gamma_c^{-p+1}}{-p+1} \right) \right]. \end{aligned} \quad (\text{B3})$$

P_{ν_1, ν_2} can then be expressed (without dependence on A) as

$$P_{\nu_1, \nu_2} = \frac{E_e \gamma_c \frac{4}{3} \sigma_T c B^2 \left(\gamma_2^{-p+2} - \gamma_1^{-p+2} \right)}{8\pi m_e c^2 (-p+2) \left[\frac{\gamma_c^{-p+2} - \gamma_m^{-p+2}}{-p+2} + \gamma_c \frac{\gamma_{\max}^{-p+1} - \gamma_c^{-p+1}}{-p+1} \right]}. \quad (\text{B4})$$

Rearranging the above expression in terms of E_e , if we assume the equipartition of magnetic and particle energy density, the magnetization σ can be expressed as

$$\begin{aligned} \sigma &= \frac{\frac{B^2}{8\pi} V}{E_e} \\ &= \frac{B^2 V}{8\pi} \frac{\gamma_c \frac{4}{3} \sigma_T c B^2 (\gamma_2^{-p+2} - \gamma_1^{-p+2})}{8\pi m_e c^2 P_{\nu_1, \nu_2} (-p+2) \left[\frac{\gamma_c^{-p+2}}{-p+2} + \gamma_c \frac{\gamma_{\max}^{-p+1} - \gamma_c^{-p+1}}{-p+1} \right]} \end{aligned} \quad (\text{B5})$$

where V is the volume of the radiating electrons. Substituting $\gamma = (2\pi m_e c \nu / q_e B)^{1/2}$, the above expression can be rewritten to obtain the magnetic field:

$$B = \left(\frac{\sigma (8\pi)^2}{V} \frac{(q_e m_e c)^{1/2} P_{\nu_1, \nu_2} (-p+2)}{\frac{4}{3} \sigma_T (2\pi \nu_c)^{1/2}} \right. \\ \left. \frac{\nu_c^{(-p+2)/2} - \nu_m^{(-p+2)/2}}{-p+2} + \nu_c^{(1/2)} \frac{\nu_{\max}^{(-p+1)/2} - \nu_c^{(-p+1)/2}}{-p+1}}{\nu_2^{(-p+2)/2} - \nu_1^{(-p+2)/2}} \right)^{2/7} \quad (\text{B6})$$

When $\nu_{\max} \gg \nu_m$, the ν_{\max} term becomes negligible, and the expression can be simplified to

$$B \approx \left[\frac{\sigma (8\pi)^2}{V} \frac{(q_e m_e c)^{1/2} P_{\nu_1, \nu_2}}{\frac{4}{3} \sigma_T (2\pi \nu_c)^{1/2}} \right. \\ \left. \left(\frac{-\nu_c^{(-p+2)/2}}{-p+1} - \nu_m^{(-p+2)/2}}{\nu_2^{(-p+2)/2} - \nu_1^{(-p+2)/2}} \right) \right]^{2/7} \quad (\text{B7})$$

Thus the magnetic field estimate is insensitive to ν_{\max} .

Following the same approach will yield the magnetic field strength for the globally fast cooling case, in which the electron SED can be described by

$$\frac{dN}{d\gamma} = \begin{cases} A\gamma^{-2}, & \gamma_c < \gamma < \gamma_m \\ A\gamma_m^{p-1}\gamma^{-p-1}, & \gamma_m < \gamma < \gamma_{\max} \end{cases} \quad (\text{B8})$$

assuming $\nu_c < \nu_m < \nu_1 < \nu_2$. Evaluating the above expressions for P_{ν_1, ν_2} and E_e using the fast cooling electron SED (the previous equation) gives

$$P_{\nu_1, \nu_2} = A\gamma_m^{p-1} c \frac{4}{3} \sigma_T \frac{B^2 \gamma_2^{-p+2} - \gamma_1^{-p+2}}{8\pi} \quad (\text{B9})$$

and

$$E_e = A m_e c^2 \left[\log \gamma_m - \log \gamma_c + \gamma_m^{p-1} \frac{\gamma_{\max}^{-p+1} - \gamma_m^{-p+1}}{-p+1} \right]. \quad (\text{B10})$$

Similarly, P_{ν_1, ν_2} can be rewritten as

$$P_{\nu_1, \nu_2} = \frac{E_e \gamma_m^{p-1} c^4 \sigma_T \frac{B^2}{8\pi} (-p+2)^{-1} (\gamma_2^{-p+2} - \gamma_1^{-p+2})}{m_e c^2 \left[\log \gamma_m - \log \gamma_c + \gamma_m^{p-1} \frac{\gamma_{\max}^{-p+1} - \gamma_m^{-p+1}}{-p+1} \right]}. \quad (\text{B11})$$

It then follows (from expanding $\sigma = (B^2/8\pi)V/E_e$ and rearranging) that

$$B = \left(\frac{\sigma(8\pi)^2}{V} \frac{(q_e m_e c)^{1/2} P_{\nu_1, \nu_2} (-p+2)}{\frac{4}{3} \sigma_T (2\pi)^{1/2} \nu_m^{(p-1)/2}} \right. \\ \left. \left[\log \left(\frac{\nu_m^{1/2}}{\nu_c^{1/2}} \right) + \nu_m^{(p-1)/2} \left(\frac{\nu_{\max}^{(-p+1)/2} - \nu_m^{(-p+1)/2}}{-p+1} \right) \right] \right)^{2/7} \\ \frac{\nu_2^{(-p+2)/2} - \nu_1^{(-p+2)/2}}{\nu_2^{(-p+2)/2} - \nu_1^{(-p+2)/2}}. \quad (\text{B12})$$

Similarly, when $\nu_{\max} \gg \nu_m$, the ν_{\max} term in the numerator becomes negligible, and the expression can be simplified to

$$B \approx \left[\frac{\sigma(8\pi)^2}{V} \frac{(q_e m_e c)^{1/2} P_{\nu_1, \nu_2} (-p+2)}{\frac{4}{3} \sigma_T (2\pi)^{1/2} \nu_m^{(p-1)/2}} \right. \\ \left. \left(\frac{\log \left(\frac{\nu_m^{1/2}}{\nu_c^{1/2}} \right) - \frac{1}{-p+1}}{\nu_2^{(-p+2)/2} - \nu_1^{(-p+2)/2}} \right) \right]^{2/7}. \quad (\text{B13})$$

REFERENCES

- Abdo, A. A., Ajello, M., Allafort, A., et al. 2013, ApJS, 208, 17
 Atoyan, A. M., & Aharonian, F. A. 1996, MNRAS, 278, 525
 Auchettl, K., Slane, P., Roman, R. W., et al. 2015, ApJ, 802, 68
 Beniamini, P., Kumar, P. 2016, MNRAS, 457L, 108B
 Buccieri, R., Bennett, K., Bignami, G. F., et al. 1983, A&A, 128, 245
 Bucciantini, N., Amato, E., & Del Zanna, L. 2005, A&A, 434, 189
 Bühl, R., & Giomi, M. 2016, MNRAS, 462, 2762
 Bykov, A. M., Amato, E., Petrov, A. E., Krassilchikov, A. M., & Levenfish, K. P. 2017, Space Sci. Rev., 207, 235
 Camilo, F., Manchester, R. N., Gaensler, B. M., & Lorimer, D. R. 2002, ApJ, 579, L25
 Cappellari, M., & Copin, Y. 2003, MNRAS, 342, 345
 Chevalier, R. A. 2005, ApJ, 619, 839
 Cordes, J. M., & Lazio, T. J. W. 2002, arXiv:astro-ph/0207156
- Cox, A. N. 2000, Allen's Astrophysical Quantities
 Crossley, J. H., Sjouwerman, L. O., Fomalont, E. B., & Radziwill, N. M. 2007, Bulletin of the American Astronomical Society, 39, 132.03
 Dame, T. M. 1993, Back to the Galaxy, 278, 267
 Diehl, S., & Statler, T. S. 2006, MNRAS, 368, 497
 Fierro, J. M., Arzoumanian, Z., Bailes, M., et al. 1995, ApJ, 447, 807
 Gaensler, B. M., van der Swaluw, E., Camilo, F., et al. 2004, ApJ, 616, 383
 Gaensler, B. M., & Slane, P. O. 2006, ARA&A, 44, 17
 Gutermuth, R. A., & Heyer, M. 2015, AJ, 149, 64
 Hales, C. A., Gaensler, B. M., Chatterjee, S., van der Swaluw, E., & Camilo, F. 2009, ApJ, 706, 1316
 Hyman, S. D., Lazio, T. J. W., Kassim, N. E., et al. 2005, Nature, 434, 50
 Intema, H. T., Jagannathan, P., Mooley, K. P., & Frail, D. A. 2017, A&A, 598, A78
 Kargaltsev, O., & Pavlov, G. G. 2008, 40 Years of Pulsars: Millisecond Pulsars, Magnetars and More, 983, 171
 Kargaltsev, O., & Pavlov, G. G. 2010, X-ray Astronomy 2009: Present Status, Multi-Wavelength Approach and Future Perspectives, 1248, 25
 Kargaltsev, O., Klingler, N., Chastain, S., & Pavlov, G. G. 2017, arXiv:1711.02656
 Klingler, N., Kargaltsev, O., Rangelov, B., et al. 2016, ApJ, 828, 70 (a)
 Klingler, N., Rangelov, B., Kargaltsev, O., et al. 2016, ApJ, 833, 253 (b)
 Manchester, R. N., Hobbs, G. B., Teoh, A., & Hobbs, M. 2005, AJ, 129, 1993
 Mori, K., Burrows, D. N., Hester, J. J., et al. 2004, ApJ, 609, 186
 Mori, H., Maeda, Y., Pavlov, G. G., Sakano, M., & Tsuboi, Y. 2005, Advances in Space Research, 35, 1137
 Morlino, G., Lyutikov, M., & Vorster, M. 2015, MNRAS, 454, 3886
 Muslimov, A. G., & Harding, A. K. 2004, ApJ, 606, 1143
 Pierbattista, M., Harding, A. K., Gonthier, P. L., & Grenier, I. A. 2016, A&A, 588, A137
 Piran, T. 2004, Reviews of Modern Physics, 76, 1143
 Posselt, B., Pavlov, G. G., Slane, P. O., et al. 2017, ApJ, 835, 66
 Predehl, P., & Kulkarni, S. R. 1995, A&A, 294, L29
 Reynolds, S. P., Pavlov, G. G., Kargaltsev, O., et al. 2017, Space Sci. Rev., 207, 175
 Romani, R. W., Ng, C.-Y., Dodson, R., & Brisken, W. 2005, ApJ, 631, 480
 Romani, R. W., & Watters, K. P. 2010, ApJ, 714, 810
 Sari, R., Piran, T., & Narayan, R. 1998, ApJ, 497L, 17S
 Taylor, J. H., & Cordes, J. M. 1993, ApJ, 411, 674
 Uchida, K., Morris, M., & Yusef-Zadeh, F. 1992, AJ, 104, 1533
 Xu, S., Yang, Y.-P., & Zhang, B. 2017, arXiv:1711.03943
 Yao, J. M., Manchester, R. N., & Wang, N. 2017, ApJ, 835, 29
 Yusef-Zadeh, F., & Bally, J. 1987, Nature, 330, 455
 Yusef-Zadeh, F., & Bally, J. 1989, The Center of the Galaxy, 136, 197
 Yusef-Zadeh, F., & Gaensler, B. M. 2005, Advances in Space Research, 35, 1129
 Zabalza, V. 2015, 34th International Cosmic Ray Conference (ICRC2015), 34, 922